ABSTRACT

Title of Document: SMOKE POINTS OF MICROGRAVITY AND NORMAL GRAVITY COFLOW DIFFUSION FLAMES

Keenan Thomas Dotson, M.S., 2009

Directed By: Assistant Professor, Peter B. Sunderland, Department of Fire Protection Engineering

Smoke points were measured in microgravity aboard the International Space Station (ISS) as part of the Smoke Points in Coflow Experiment (SPICE), and in normal gravity conditions. In microgravity conditions increasing the coflow velocity or decreasing the burner diameter increased the smoke point flame length. A simplified prediction of centerline jet velocity did not yield residence-time-based criticalities or data collapse. Simulation of non-reacting flows showed that the simplified centerline velocity prediction was able to predict velocity decay for only relatively weak coflows. An improved model may yield different results. In normal earth gravity coflow velocity exhibited mixed effects. For burner diameters of 0.41, 0.76, and 1.6 mm, smoke points increased with increases of coflow velocity. For an unconfined coflow burner with a burner diameter of 13.7 mm smoke point length decreased with increasing coflow velocity for ethylene and propylene, while increasing for propane flames.

SMOKE POINTS OF MICROGRAVITY AND NORMAL GRAVITY COFLOW DIFFUSION FLAMES

By

Keenan Thomas Dotson

Thesis submitted to the Faculty of the Graduate School of the
University of Maryland, College Park, in partial fulfillment
of the requirements for the degree of
Master of Science
2009

Advisory Committee:
Assistant Professor Peter B. Sunderland, Chair
J. L. Bryan Professor James G. Quintiere
Associate Professor André W. Marshall

ProQuest LLC
789 East Eisenhower Parkway
P.O. Box 1346
Ann Arbor, MI 48106-1346

Acknowledgements

Many have helped me along the way during the production of this thesis. First and foremost none of this would have been possible without the support and guidance of my advisor, Dr. Peter B. Sunderland. I relied heavily on his knowledge and experience to guide me through a many of unknown territories in my current foray in graduate research and study. I hope that one day I will become just as passionate about my work as he is.

I would also like to acknowledge the collaborators on this project David L. Urban and Zeng-Guang Yuan at NASA Glenn Research Center and the National Center for Space Exploration and Research. Their significant contribution to obtaining the data was essential to obtaining the microgravity flame data. I am deeply indebted to them as I was not the one who had to show up at 4 am in the morning to guide astronauts in finding smoke points. Our weekly teleconference meetings were very helpful in guiding my work and obtaining much feedback on my results and writings. Zeng-Guang deserves special notice for designing and performing the COMSOL® simulation that I report on in this thesis. It was an essential part for evaluating the analytical model.

This research was supported by NASA cooperative agreement NNX07AO91A and the Department of Fire Protection Engineering at the University of Maryland. This project would not have happened if it were not for the late Gerard M. Faeth of the University of Michigan, who inspired this work. Also deserving of thanks are the

SPICE engineering team, including Jay Owens, Charles Brunell, Tibor Lorik; the ISS and MSG Operations teams; and the ISS crew members that conducted the tests Michael Barratt, E. Michael Fincke, Sandra H. Magnus, and Koichi Wakata.

On a more personal note, I do not believe I could have maintained by sanity during my graduate studies without helpful and encouraging discussions with friends and family. Vivien Lecoustre and Praveen Narayanan were always willing to lend advice when I felt I had reached a dead-end. My parents, Renee and Richard Dotson, and my brothers, Stuart and Taylor Dotson, were there to encourage my work and relate their relevant experiences. My wonderfully caring girlfriend Cristel Thomas was on the frontline with me. She was always available to listen and hearten me when I needed it the most.

Table of Contents

List of Tables

List of Figures

Chapter 1. Introduction

Soot formation is an important but unresolved problem in combustion science. In many circumstances soot production in flames is desired. Nevertheless, once soot escapes the flame and becomes smoke, it is rarely if ever wanted in a combustion system. Soot is estimated to be responsible for up to 52,000 premature deaths in the U.S.[1] and is believed to contribute to climate change and glacial melting.[2] Radiation from soot in flames allows reading by candlelight, provides heat to campers, and cooks our food. On the other hand this radiation can represent a loss of efficiency and increased heat loads in engines. Also the spread of unwanted fires is in many cases is through the radiation heat transfer originating from soot particles. Smoking flames emit carbon monoxide, which is the major cause of death in fires.[3]

1.1. Smoke Point

The laminar smoke point is the condition (or luminous flame length) where a laminar diffusion flame begins to emit soot. Smoke points are the prevalentmethod used to determine fuel sooting propensity in diffusion flames. The longer the luminous (visible) flame length at its smoke point, the lower the sooting propensity of the fuel. In normal gravity, laminar smoke points have been measured for many gaseous and condensed fuels.[4-6, 7-9] Laminar smoke points have been found to correlate with soot volume fractions[10] and radiative loss fractions[11] of turbulent diffusion flames. Yang et al.[12] found that gas turbine soot emissions correlate with a threshold sooting index (TSI) based on fuel molecular weight divided by the laminar smoke point. Smoke points have been shown to correlate with the smoke release from turbulent buoyant

flames,[13] and have been applied to developing general soot models for computation combustion simulations[14] and heat release measurements.[15]

Smoke points for gaseous fuels are determined from a jet flame apparatus. A surrounding coflow of excess oxidant (over-ventilated conditions) is typically necessary for buoyant flames to reduce flame flickering. It is also most common to confine the coflow and jet within a quartz chimney to reduce disturbances from exterior flows. Shorter smoke point flame lengths are indicative of a higher sooting propensity. A flame that has a lower inclination to form soot will exhibit a smoke free flame for longer flame lengths; that is longer flame residence times are required to create the necessary amount of soot to reach the smoke point condition.

1.2. Soot Formation, Growth, and Oxidation

General consensus has that the soot formation process begins with the formation of polycyclic aromatic hydrocarbons (PAHs). From these precursors fine soot particles nucleate. These particles grow by addition of PAHs or through surface reactions. The Hydrogen Abstraction by Carbon (Acetylene) Addition (HACA) mechanism is one of the most often cited for soot growth mechanisms. In addition, coagulation, in which small particles coalesce into larger particles and agglomeration, where multiple particles combine into larger pearl-necklace-like structures, also contribute to morphology. Soot oxidation occurs from participation from species such as O_2, O, and OH present near and downstream of the flame sheet. OH-based oxidation is the most dominant soot oxidation mechanism, occurring from slightly rich to lean

conditions within the flame. O_2-based oxidation becomes more important as the flame becomes leaner and the super-equilibrium levels of OH decline.[16] Both soot formation and soot oxidation are temperature dependent.

Detailed measurements have provided greater insight into sooting phenomena. In premixed ethylene flames, Harris and Weiner[17,18] determined that soot reaches a final particle size due to a decrease in reactivity of the particle that stops surface growth, and the dominate growth mechanism is by acetylene. In diffusion flames Kent et al.[19,20] have shown that soot particles are formed primarily on the fuel side of the flame reaction zone. The number of particles decreases by coagulation away from the peak formation zone (a few millimeters inside the reaction zone on the fuel side), while particle size and soot volume fraction increase by the addition of hydrocarbon species. Soot typically convects towards the fuel side of the flame after it has formed from buoyancy. The soot path ultimately follows on the local streamlines. Thermophoretic forces modify these paths slightly towards cooler regions within the flame.

Santoro et al.[21,22] discovered a unique feature of coflow diffusion flames. The annular region near the base of the flame is a location of intense nucleation and agglomeration of soot. This formation region is the cause of the soot 'wings' seen in diffusion flames near their smoke points. Gomez et al.[23] found that soot formation begins at a temperature around 1350 K in diffusion flames and that dilution does not change this temperature but rather shifts the location at which this temperature

occurs. Sunderland and Faeth[24] determined soot nucleation to become significant at 1250 K. Kent and Wagner[25] found that smoke burnout in the oxidative region of the flame ceases when the tip of a buoyant diffusion flame cools to approximately 1300 K. This is the direct cause of the smoke point flame. Urban et al.[26] found that the luminous tip of a nonbuoyant (microgravity) flame reaches 1000 K at its smoke point. In buoyant flames this decrease in temperature is attributed primarily to heat conduction, and in nonbuoyant flames this can be significantly enhanced by radiative quenching.[16] Radiative quenching is believed to also cause the visible tip opening in nonbuoyant smoke points of flames of relatively long residence times.[26]

In diffusion flames, oxygen and fuel meet at a narrow reaction zone, the flame sheet. Kinetics does not determine the location or temperature of this zone, but rather stoichiometry does. Diffusion limits the flow of the reactants to this narrow flame sheet and, for strong flames, is much slower than the kinetic reaction rate. Furthermore the soot formation/oxidation times are believed to be greater than the time necessary for diffusion of reactants.[27] If chemical kinetics is practically instantaneous, then residence time becomes the determining factor for soot formation and oxidation. It has also been suggested that the ratio of soot formation and soot oxidation times also determines when the smoke point will occur. Lautenberger et al.[27] describe this process for buoyant laminar flames. “Increasing the flame height increases the residence time and allows more time for the flame to produce soot. Once formed, this soot requires additional time to oxidize in the upper parts of the

flame if it is to be entirely consumed below the flame tip. As soot travels through the flame (in a Lagrangian sense), it radiates away energy and cools the flame gases."

Also corroborating what was mentioned previously about a limiting temperature at which soot oxidation ceases, typically at the smoke point flame height, the radiative heat loss from the flame by soot radiation is about 30% of the total heat release rate of the flame.[28] The cooled flame gases can no longer oxidize the soot and one could consider the soot formation/oxidation time to approach the diffusion time.[27] Smoke is then released from the tip of this flame and it has just surpassed its characteristic smoke point because the required time for soot oxidation is now less than the time the soot is capable of being oxidized post flame sheet.

Important review articles on soot formation mechanisms are available from Frenklach[29], Mansurov[30], and Glassman.[31] Richter and Howard[32] in a particularly detailed fashion reviewed the formation of PAHs and their growth to soot. Soot oxidation is well covered by Stanmore et al.[33]

1.3. Fuel and Diluent Effects

For diffusion flames, work by Schalla and McDonald[34] showed that fuel sooting propensity decreases with hydrocarbon family in the following order: aromatics > alkynes > alkenes> alkanes. According to Glassman[31], increasing the molecular weight of the fuel increases the soot formation rate by increasing the radical concentration and the Arrhenius pre-exponential factor for the overall rate coefficient. In premixed flames, the number of carbon-carbon (C-C) bonds determines the critical

sooting equivalence ratio in a predictable fashion. However, the number of C-C bonds is only an indirect measure of the pyrolysis rate of the fuel.

In diffusion flames H radicals are important to the fuel pyrolysis process, facilitating the initial pyrolysis of the virgin fuel as well as the subsequent attack on fuel intermediates. H radicals facilitate abstraction reactions much faster than hydrocarbon radicals do. Despite this importance of H radicals, Schug et al.[4] have shown that the initial overall carbon-hydrogen (C/H) atom ratio of the fuel does not determine the sooting propensity. Nevertheless the degree of molecular unsaturation correlates with higher sooting propensity, perhaps likely due to the greater ease these molecules can form acetylenes and PAHs.

In over-ventilated coflow diffusion flames, addition of inert to the fuel stream typically reduces sooting propensity. Longer smoke points result. However the addition of inert can also alter the flame temperature. This occurs by the inert acting as a heat sink, this effect depending on the heat capacity of the inert.[4,35] The peak flame temperatures will be reduced, which for a diffusion flame reduces soot formation, increasing the smoke point. Additionally, the temperature field of the flame can be altered through transport effects. Inert species with high thermal diffusivities have their volumetric dilution effects countered by a thermal effect of extending the high temperature range where soot formation is possible.[36] The temperature of the pyrolysis zone determines the soot propensity and correlates well

the fuel mass flow rate at the smoke height. Shock tube experiments have shown that the soot formation rate peaks around 1900 – 2300 K.[31]

1.4. Buoyancy Effects

Soot is transported in flames primarily by convection, modified slightly by thermophoresis. The primary difference between a buoyant and nonbuoyant jet flames is that, in general, a buoyant flame, the flow is accelerating, while for a nonbuoyant jet the flow is decelerating. This is of course neglecting volumetric expansion from combustion related heating. In general, for a buoyant flame the flow streamlines move towards the flame axis, while for the nonbuoyant flame the flow streamlines are drawn outwards from the flame axis.[16] Therefore in a buoyant flame, once soot is nucleated in the soot production region near the flame sheet, it is drawn into the fuel rich core, allowing continued growth. In a nonbuoyant flame as the flow is drawn outwards, the soot moves in a more direct path to the flame sheet and oxidative region downstream.[16]

It had been predicted that smoke points would not occur in nonbuoyant gas-jet flames.[37] This was based on the assumption that residence time would be independent of flow rate in microgravity flames. As flame length and mass flow rate are directly proportional, an increase in velocity would lead to proportional increase in length and residence time would remain unchanged. In normal gravity flames the residence time scales with the square root of the flow rate. Subsequent work[38] observed smoke points of nonbuoyant flames aboard a parabolic aircraft and used numerical predictions to

show that residence time increases with flame length for nonbuoyant flames without coflow. Urban et al.[39] reported smoke points of microgravity flames observed on a space shuttle. However, microgravity smoke point measurements are difficult in parabolic aircraft owing to g-jitter and in drop facilities owing to limited test times.

1.5. Velocity Field Effects

By varying the burner diameter, coflow velocity, and fuel dilution, flame shape and residence times in the soot formation and soot oxidation regions can be changed. Reductions in the burner (fuel jet exit) diameter increase the mean fuel jet velocity, reducing overall flame residence time, assuming that flame length only depends on the mass flow rate of fuel. There has not been substantial research into the burner diameter effect on smoke points. The work of Kent and Wagner[25] showed that reducing burner diameter (increasing fuel jet velocity) shifts the centerline soot-volume-fraction profile downstream, without modifying peak values. Therefore it should be expected that the smoke point luminous flame length should increase from the soot profile shifting downstream, directly lengthening the flame or reducing the region of the flame where soot formation is possible. Increasing fuel dilution, in addition to modifying soot propensity by volumetric and thermal effects, increases the fuel jet velocity at a particular mass flow rate of hydrocarbon fuel.

An increase in coflow velocity will generally decrease entrainment towards the flame axis. The coflow velocity can modify the residence time by countering flow deceleration in nonbuoyant flames, and accelerating flow in both nonbuoyant and

buoyant flames. Nonbuoyant flames are substantially more likely to have their velocity fields modified by these previously mentioned factors as their flow is not subject to buoyancy related acceleration, which can tend to dominate the flow field.[16]

Schalla and McDonald[34] were the first to investigate the effects of coflow velocity on the smoke point of laminar diffusion flames. Their work showed that increasing coflow velocity increased the fuel mass flow rate at the smoke point up to a point, after which the effect ceases. A modified plot of their results is shown in Figure 1.1. Berry-Yelverton and Roberts[40] showed that the smoke point of ethylene increased with decreasing initial fuel to air velocity ratio, and therefore with increasing coflow velocity, as shown in Figure 1.2. These tests were over a range of fuel/air velocity ratios, 0.6 - 1.4. The results of Schalla and McDonald were also over an initial fuel to

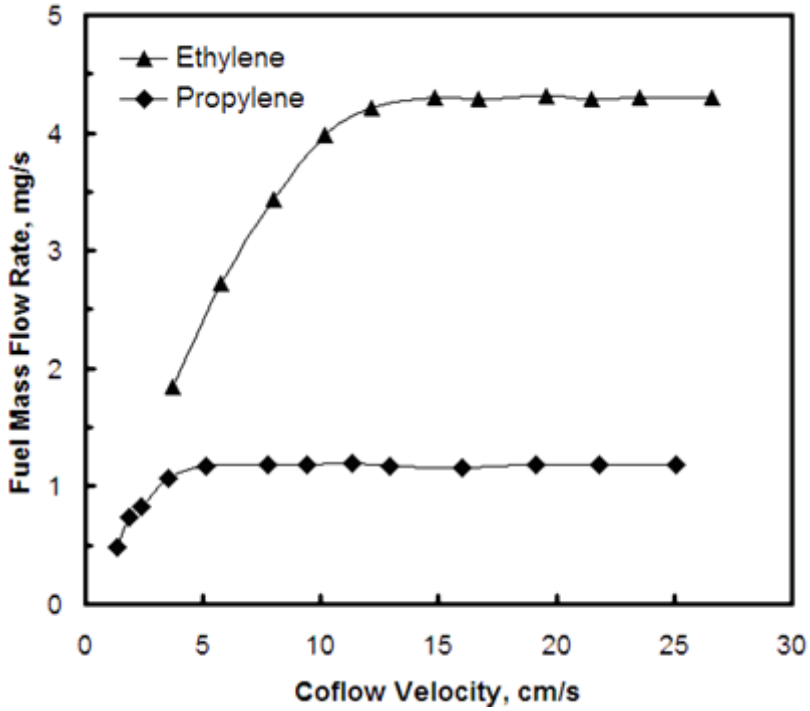

Figure 1.1. Variation of maximum smoke free fuel flow (smoke point) with coflow velocity. Burner inner diameter (ID) of 9 mm. Adapted from Schalla and McDonald.

air velocity ratio of 0.14 - 0.42 for ethylene, where higher numbers indicate lower relative coflows. Note that Berry Yelverton and Roberts obtained their results with a larger fuel burner, 11.9 mm, than Schalla and McDonald, 9 mm.

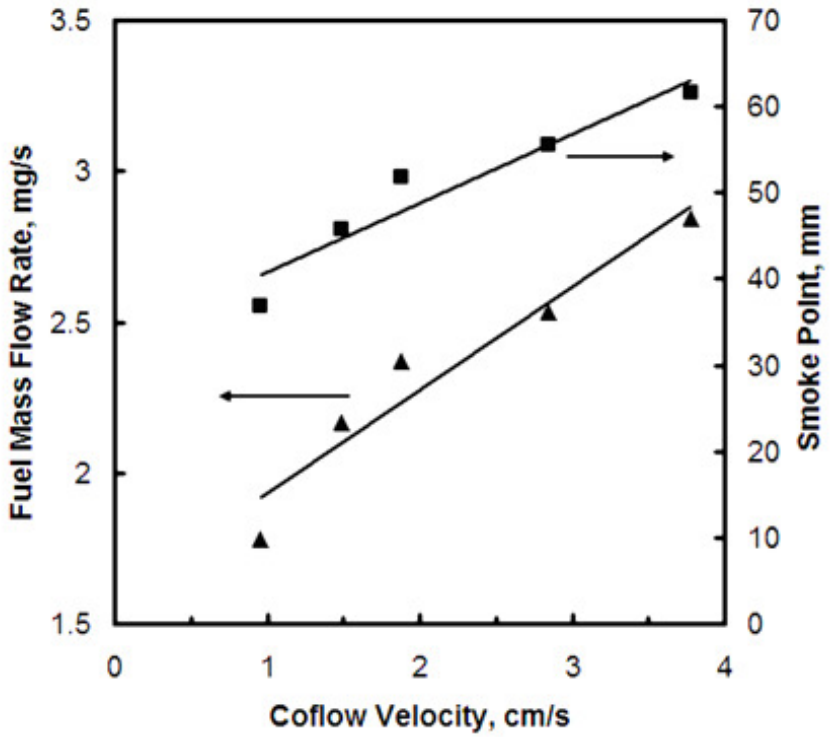

Figure 1.2. Dependence of the smoke point of ethylene on coflow velocity. Burner ID of 11.9 mm. Adapted from Berry-Yelverton and Roberts.

A recent 2.5 s drop tower study by Jeon et al.[41] found that for small coflow velocities the soot volume fraction increases with coflow velocity for nonbuoyant flames. The study was of ethylene flames with a 7 mm burner. This was attributed to an increase in flame temperatures as luminosity increased in the annular regions of the flame. They reasoned that the increase in forced flow of oxidizer increased the rate of the reaction of the combusting species, and this supposition is somewhat supported by the observed decrease in flame length. Though not noted in their article, these flames are

believed to be smoking heavily as indicated by their color images and comparison to smoke points found here.

Lin and Faeth[7,42] studied the effects of coflow velocity on weakly-buoyant flames near their smoke points. They studied a variety of fuels exiting from a 6 mm burner. Flames were observed in normal gravity but at low pressures to reduce the effects of buoyancy. It was not possible to obtain smoke point flame lengths as a function of coflow velocity; however fuel mass flow rates are shown in Figure 1.3. They found that increasing the coflow velocity reduced soot volume fractions and increased the smoke point length, similar to previous studies. This was attributed to decreased flame residence time and modified soot pathlines. Refs. 7 and 41 both showed that luminous flame lengths decrease with increasing coflow velocity.

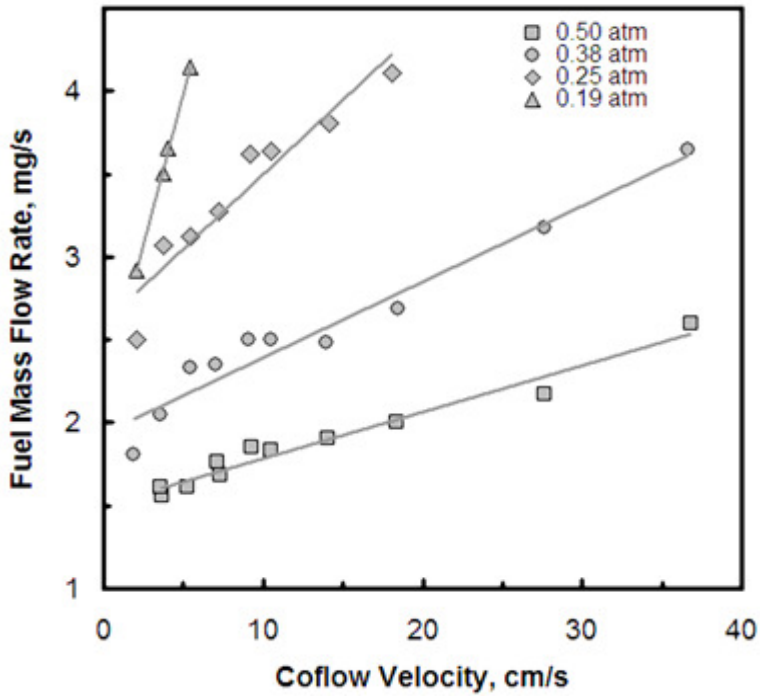

Figure 1.3. Smoke point fuel flow rates as a function of coflow velocity for weakly buoyant propylene flames at a variety of pressures. Burner ID is 6 mm. Adapted from Lin and Faeth.

Chapter 2. Theoretical and Numerical Methods

2.1. Flame Shapes

Faeth and co-workers[42 - 44] applied the flame shape analysis of Spalding[45] to still flames. This is a similarity solution approach that assumes the following for a steady, axisymmetric laminar jet diffusion flame at constant pressure in a still environment: (1) no buoyant forces (2) no viscous dissipation (low Mach number), (3) the flame has a large aspect ratio so that diffusion of species, momentum and energy in the streamwise direction is small, (4) all chemical reactions occur in a thin flame sheet with an infinite reaction rate, (5) diffusivities of mass of all species, momentum, and energy are all equal (unity Lewis number), (6) all transport properties and heat capacities are constant and equal throughout the flame, (7) effects of radiation are small, and (8) constant density. An additional caviot is that rather than matching the initial conditions at the jet exit, integral conservation of species is maintained. This approach is more suited to predicting conditions in the far-field where similarity is likely to be satisfied.

Conservation of mixture fraction, f, for an axisymmetric flow, is

$$u_z \frac{\partial f}{\partial z} + u_r \frac{\partial f}{\partial r} = \frac{\nu}{r} \frac{\partial}{\partial r}\left(r \frac{\partial f}{\partial r} \right), \tag{2.1}$$

where u_z, u_r are the axial and radial velocity components in the z and r directions respectively. Kinematic viscosity is designated here as ν. Assuming the similarity variable, η,

$$\eta = \frac{r}{z}, \tag{2.2}$$

with boundary condition that $f = 0$ as $z \rightarrow \infty$, using the integral constraint

$$\int_0^{\infty} u_z f \,(2\pi r)\, dr \;=\; \frac{\pi d^{\,2} u_{f,o} f_{f,o}}{4}, \tag{2.3}$$

where d is burner diameter and subscript f,o denote initial fuel stream properties. Evaluating the result at $f = Z_{st}$, the stoichiometric mixture fraction, results in the following equation for flame length, L_f:

$$\frac{L_f}{d} = \frac{3\,\mathrm{Re}}{32 Z_{st}}, \tag{2.4}$$

where *Re* is the fuel jet Reynolds number. Lin et al.[43] relaxed the assumption of equal diffusivities by introducing the Schmidt number, *Sc*, considering this number to primarily affect mass transport in the flame, adding a fine tuning coefficient of C_f, and including a virtual origin correction factor of L_o to account for lack of agreement for low aspect ratio flames, resulting in

$$\frac{L_f - L_o}{d} = \frac{3 C_f \,\mathrm{Re}\, Sc}{32 Z_{st}}. \tag{2.5}$$

The approach of Mahalingam et al.[46] to nonbuoyant gas-jet flames in coflow proceeds in the same fashion with similar assumptions. Additionally, radial velocity

is neglected and the axial velocity is assumed to be constant and uniformly the coflow velocity. The starting equation, as presented by Lin and Faeth,[42] is

$$u_{a,o}\frac{\partial f}{\partial z}=\frac{\nu}{r}\frac{\partial}{\partial r}\left(r\frac{\partial f}{\partial r}\right). \tag{2.6}$$

Here the subscript *a,o* denote initial air stream properties. Assuming the similarity variable to be

$$\eta=\frac{u_{a,o}r^2}{\nu z}, \tag{2.7}$$

with boundary condition that $f = 0$ as $z \rightarrow \infty$, using the integral constraint

$$\int_0^\infty u_{a,o} f\,(2\pi r)dr=\frac{\pi d^2 u_{f,o} f_{f,o}}{4}, \tag{2.8}$$

and evaluating the result at $f = Z_{st}$, the stoichiometric mixture fraction, results in

$$\frac{L_f}{d}=\frac{\mathrm{Re}}{16Z_{st}}. \tag{2.9}$$

Lin and Faeth relaxed assumptions in a similar manner as described for Equation (2.5) to obtain

$$\frac{L_f-L_o}{d}=\frac{C_f\,\mathrm{Re}\,Sc}{16Z_{st}}, \tag{2.10}$$

for the coflowing case. The Schmidt number and viscosity in Equations (2.5) and (2.10), and the Reynolds number contained within were those of air at the mean of the adiabatic flame temperature and the ambient temperature.

Schmidt number and viscosity, defined in this fashion, do not vary substantially for the flames in this study, and are not considered significant. In addition the virtual origin correction is neglected, at least initially. With this in mind, Equations (2.5) and (2.10) can be arranged to

$$L_f = C\dot{m}_f / Z_{st} \,, \tag{2.11}$$

to indicate the general proportionality the should be expected from laminar jet flames in still and coflowing air. Here C is a constant and $\dot{m}_f$ is the fuel mass flow rate from the burner. It should be noted that the previous derived equations for flame length are for the stoichiometric flame length, and they are have been applied to the luminous flame length, assuming that the luminous flame length is around twice that of the stoichiometric flame length at the smoke point.

2.2. *Smoke Point Scaling*

Attributing smoke point behavior to total residence time helps with qualitative explanations of smoke point behavior but to date has not yielded successful quantitative correlations.[8] This may be because smoke points arise from a competition between the times available for soot formation and soot oxidation. Delichatsios and co-workers[47,48] suggested that smoke point length is proportional to soot formation

time. Quantitative correlations may also be possible from an examination of radiative losses, which have been observed to be 20-30% for normal-gravity smoke point flames and increase with adiabatic flame temperature.[5]

As a first approximation, the velocity field of a non-reacting axisymetic jet flow was investigated to estimate residence times for the microgravity flames in this study. Much of the literature assumes constant velocities throughout the flow field of jet flames for residence time estimation. It is more appropriate to consider theoretical velocity decay from a jet. There has not been an adequate theory developed for the velocity field of a laminar jet in coflow. The literature focuses on jets into a still environment (simple jets),[49 - 54] urbulent jets in a slow moving coflow[55], or even jets in a counterflowing stream[56]. The only experimental study on jets in a coflowing stream (including jets in the laminar regime) utilized contraction nozzles to produce an initial uniform velocity profile (plug flow), rather than fully developed Poiseuille flow.[57]

Here the velocity decay on the jet centerline will be determined by adaptation of the similarity solution developed by Schlichting[58] for simple laminar jets, which can be found in his original work, or any number of combustion or fluid mechanics texts. The manner of solution is a similarity solution analogous to that of the Spalding solution of the conservation of mixture fraction presented in Section 2.1. Starting from the conservation of momentum for an axisymmetric jet

$$u_z \frac{\partial u_z}{\partial x} + u_r \frac{\partial u_r}{\partial r} = \frac{\nu}{r} \frac{\partial}{\partial r}\left(r \frac{\partial u_z}{\partial r} \right), \tag{2.12}$$

As $r \rightarrow \infty$, $u = 0$, and at z = 0, $u_r = 0$, $\partial u_x / \partial r = 0$ and u_z is nonzero only within the burner. Also the integral condition

$$J = \int_0^\infty \rho u_z^2 (2\pi r) dr \ , \tag{2.13}$$

is assumed to be conserved throughout the flow (ρ is the jet fluid density and J is the axial jet momentum). The similarity solution matches the integral condition rather than the boundary conditions at the jet exit. J can be determined from the initial jet velocity profile between zero and the inner wall of the burner. The resulting similarity solution for the jet centerline velocity, u_{cl}, is

$$u_{cl} = \frac{3J}{8\pi\mu}\left(\frac{1}{z}\right), \tag{2.14}$$

where μ is the exterior fluid dynamic viscosity and z is axial direction. For fully developed flow, the velocity profile is $u_z = 2u_{f,o}(1\text{-}r^2/r_o^2)$ at the jet exit (r_o is the burner inner radius). Total jet momentum is then

$$J = \frac{\pi \rho u_{f,o} d^2}{6} . \tag{2.15}$$

Recall that $u_{f,o}$ is the initial, mean jet velocity. The solution assumes a point source approximation for the jet and a singularity is present at $z = 0$. Typical approaches

include a virtual origin correction to improve the prediction of velocity near the jet-exit.[50,53,59]

Only one attempt at adapting the Schlichting similarity solution has been found in the literature.[60] Due to the inability to replicate that work, the following approach will be used. Similarity of the velocity profile (as in Schlichting's solution) will not be assumed, rather similarity of the relative velocity, $u - u_{a,o}$, profile will be assumed. This has been shown to be reasonable for some turbulent jets in coflow.[61] Consider the following a simple approximation rather than a formal derivation. This modification results in,

$$u_{cl} - u_{a,o} = \frac{3J}{8\pi\mu}\left(\frac{1}{z}\right), \tag{2.16}$$

but here, jet momentum, J, cannot be the entire jet momentum, but rather the jet momentum relative to the surrounding coflow. Many different approximations for J were considered, resulting in only minor differences in the resulting velocity decay profile. We will consider here that J is,

$$J = \int_0^\infty \rho\left(u_z - u_{a,o}\right)^2 \left(2\pi r\right) dr\,, \tag{2.17}$$

$$J = \pi\rho d^2 \left(\frac{u_{f,o}^2}{3} - \frac{u_{f,o}u_{a,o}}{2} + \frac{u_{a,o}^2}{4} \right), \tag{2.18}$$

with u_z of a parabolic velocity profile, and neglecting the minor density differences between the fuel and coflowing air.

Next a virtual origin correction is applied. A virtual origin such that the centerline velocity at $z = 0$ is $2u_{f,o}$ will be assumed, that is

$$z_o = \frac{3J \big/ 8\pi\mu}{2u_{f,o} - u_{a,o}}\,. \tag{2.19}$$

where z_o is restricted to positive values. The final equation for centerline velocity on for a jet in coflow is therefore

$$u_{cl} = \frac{3J}{8\pi\mu}\left(\frac{1}{z + z_o}\right) + u_{a,o}\,. \tag{2.20}$$

Centerline residence time is found from

$$t_{res} = \int_0^L \frac{dz}{u_{cl}}\,, \tag{2.21}$$

using an integral substitution of

$$\xi = u_{a,o}(z + z_o) + \frac{3J}{8\pi\mu}, \tag{2.22}$$

to obtain

$$t_{res} = \frac{L}{u_{a,o}} - \frac{a}{u_{a,o}^2} \ln\left[\frac{u_{a,o}(L + z_o) + a}{u_{a,o} z_o + a}\right], \tag{2.23}$$

for the residence time to a particular length, L, where

$$a = \frac{3J}{8\pi\mu}. \tag{2.24}$$

2.3. *COMSOL Modeling of Air Jets in Air Coflow*

Modeling of nonreacting jets in coflow was performed in COMSOL® Multiphysics 3.5. The model solves the Navier-Stokes equations for incompressible, isothermal and nonreacting flow for a single species. Only conservation of mass and momentum were considered. At present it has only been applied to verification of the centerline velocity model developed in Section 2.2.

Two COMSOL® models were developed. The first considered an air jet with a uniform velocity of 50 cm/s entering the geometry used for the microgravity SPICE tests for the 1.60 mm burner. This uniform flow became fully developed as it progressed through the burner tube. The surrounding uniform coflow of air entered below the burner and was varied between 0 - 200 cm/s. The exit boundary condition

was a free flow boundary. The rectangular duct geometry of the SPICE module was replaced with a cylindrical geometry with equal cross-sectional area, to reduce computation time. The outer wall was at a radius of 50.8 mm from the centerline. Fluid slip was not allowed on the outer wall or on the burner surfaces. The next model removed the burner surfaces. Instead the jet was specified at the inlet. The inlet boundary conditions consisted of a parabolic (fully-developed) flow profile, $u_z = u_{f,o}(1-r^2/r_o^2)$, over a diameter of 1.60 mm ($2r_o$) about the centerline surrounded by a uniform coflow entering at the inlet boundary and varying between 0 - 200 cm/s.

Chapter 3. Experimental Procedure

All of the tests performed required determining when the smoke point condition was reached. The smoke point is a transition between two different flame behaviors, non-smoking and smoking. There are several indicators of the smoke point. A non-smoking flame does not have any obvious smoke production, and it is helpful to view the flame against a white or black background to determine this. Generally a white background it best for observing smoke production visually. A non-smoking flame has a relatively sharp luminous boundary at its luminous flame tip. This is somewhat dependent on overall soot concentrations within the flame. The tip is usually closed, though soot 'wings' are also typically present. These horn-like structures at the luminous flame tip are produced in an annular region containing the majority of the flame sheet. The luminous flame tip is also bright, and orange or yellow in color. A sooting flame usually opens up at its tip and is usually not sharply defined. The tip also darkens and becomes redder due to the cooling of the soot.

3.1. SPICE Module on ISS

The Smoke Points in Coflow Experiment (SPICE) module was brought to the International Space Station (ISS) in 2008. It was operated in the Microgravity Science Glovebox (MSG) by various crewmembers in 2009. The equipment is shown schematically in Figure 3.2 and in a photograph in Figure 3.3. Smoke points were attempted for all fuel and for fuel burner diameters of 0.4064, 0.764, and 1.600 mm. The conditions for which smoke points were found are summarized in Table 3.1. In

Table 3.1. Summary of microgravity smoke points observed.

Parameter	C_2H_4	C_3H_8	C_3H_6	75% C_3H_6	50% C_3H_6
Z_{st}	0.0637	0.0603	0.0637	0.0768	0.1018
T_{ad}, K	2367	2264	2332	2317	2288
d, mm	0.76 – 1.6	0.76 – 1.6	0.41 – 1.6	0.76 – 1.6	0.76 – 1.6
$u_{a,o}$, cm/s	18 – 58	16 – 45	5.4 – 57	13 – 65	11 – 49
L_{SP}, mm	37 – 105	46 – 105	13 – 59	15 – 44	22 – 50
$u_{f,o}$, cm/s	69.6 – 734	48.9 – 460	11.2 – 763	19.9 – 272	49.6 – 112
$\dot{m}_f$, mg/s	1.62 – 3.89	1.80 – 3.84	0.39 – 1.73	0.64 – 1.98	1.45 – 3.29
Re	127 – 636	176 – 788	36.4 – 630	49.8 – 324	89.4 – 207
# Smoke Points	6	6	20	13	7

All smoke point flames were attached to the burner, i.e., not lifted. For mixtures the fuel mole fraction is shown and the inert is N_2. Parameters $u_{a,o}$, $u_{f,o}$, and Re assume conditions of 298 K, 101 kPa and 21±1% O_2, and uniform velocity profiles. Viscosities used to calculate Re involve burner gas properties at 298 K and 101 kPa.

some cases (e.g., tests involving ethylene) the fuel supply was depleted before all the desired smoke points could be found, as the supply was limited to two 75 cc bottles of each fuel at gage pressures of 760-1440 kPa depending on the fuel.

The SPICE module, sketched in Figure 3.1, contains a rectangular duct that has an approximately 76 x 76 mm square cross-section with rounded corners. A DC fan supplies coflowing air from the glovebox contents. The air passes through a honeycomb and screen to reduce swirl and then enters the duct. The air and combustion products leave the duct through a perforated copper plate followed by a copper screen. The screen is 50 mm upstream of the burner discharge and the plate is 120 mm downstream. Fan voltage is varied to control the coflow velocity, which is measured with a hot-wire anemometer between the inlet honeycomb and screen. This anemometer was calibrated in normal gravity using a hot-wire anemometer 13 mm above the burner nozzle tip.

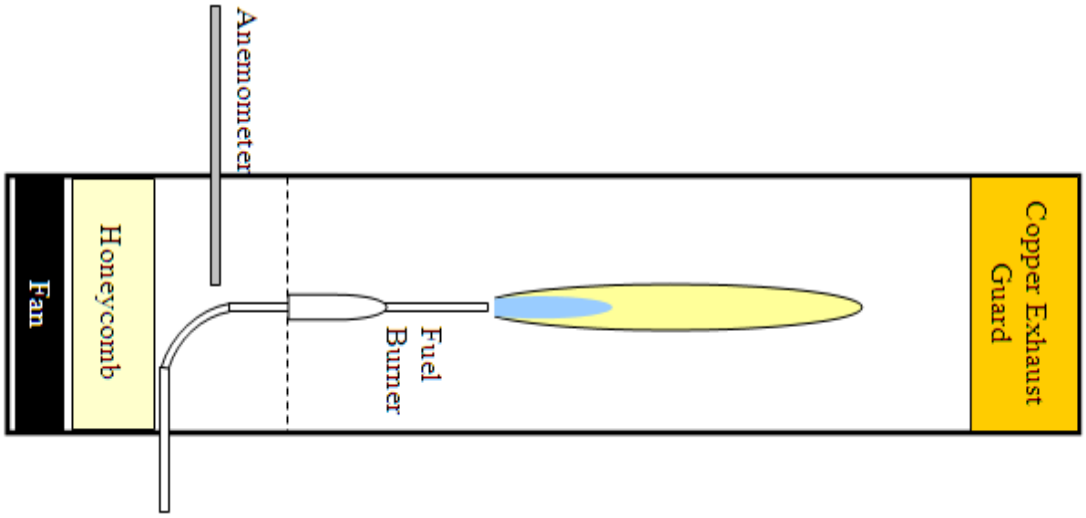

Figure 3.1. Diagram of SPICE experimental chamber. Not to scale.

Fuel flow rate was adjusted manually and controlled with an eletronic mass flow meter. The flames were ignited with a hot-wire ignitor. Video was recorded with an analog color video camera and downlinked in real time. Still images were recorded with a 12-bit Nikon™ D100 single-lens reflex color digital still camera (3008 x 2000 pixels) with a 60 mm lens.

Most tests were conducted by setting the coflow velocity, igniting the flame, and adjusting the fuel flow rate. Approximate smoke points were identified in the video by the flight crew and simultaneously by the ground support crew in Cleveland, OH. Typical burn times were 60 s, and after two of such burns, the MSG contents were flushed with ISS cabin air. The video record downlinked to NASA Glenn was recorded on a digital video disk (DVD) writer and a digital video camera (DVCAM) simultaneously. Video from the flame tests were primarily taken from the DVD, cropped and compressed (x264 encoding, 500 kbps variable bit-rate) into separate

videos for analysis. For tests that were missing from the DVD, video was taken from the DVCAM. One smoke point test was obtained from a digital screenshots taken from a computer also receiving the downlinked video. Images from this source are designated as PNG.

After the tests the video record was analyzed to identify smoke point conditions. The associated coflow and fuel flow rates were obtained from digital data recorded in the video. The smoke point lengths, L_{SP}, were obtained from the video record and are the measured distance from the burner tip to the tip of the luminous flame on the flame axis. The luminous flame tips were not sharply defined in most images, but rather involved a transition from bright yellow to black across an axial distance of 2-5 mm. Flame height was thus measured to the point where the centerline grayscale intensity changed most rapidly between these yellow and black regions. This helped reduce the

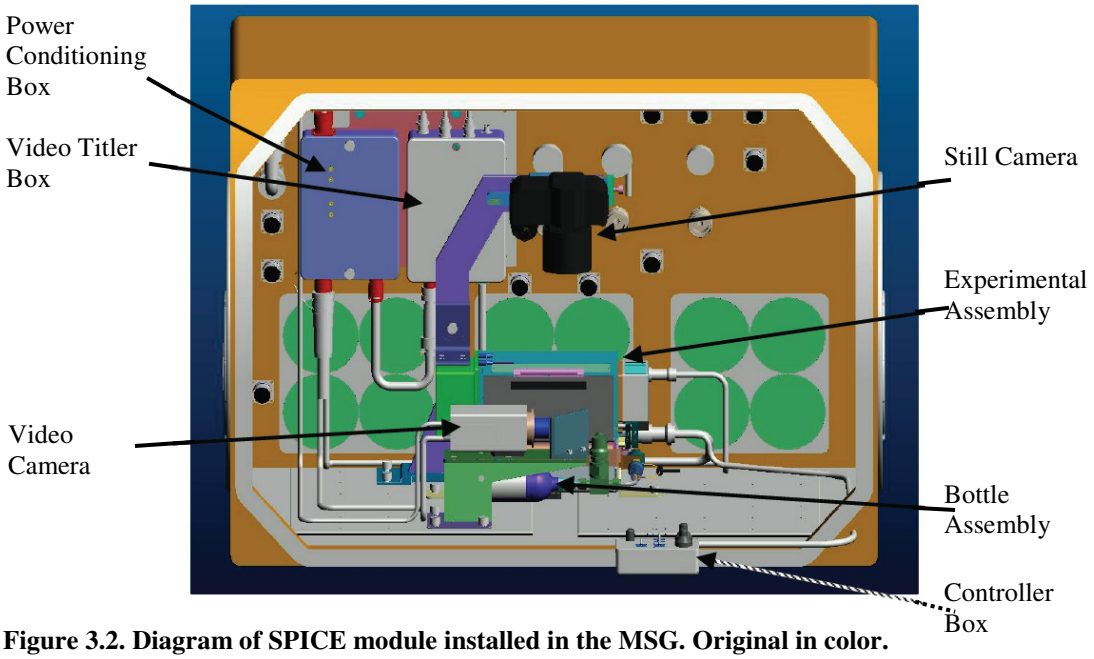

Figure 3.2. Diagram of SPICE module installed in the MSG. Original in color.

sensitivity of the measured flame length to camera exposure settings. Correlations between the measured pixel length and actual distance are given in the Appendix, organized by day of the year and image source (x264 originating from DVD or DVCAM source, DVD, DVCAM, or PNG).

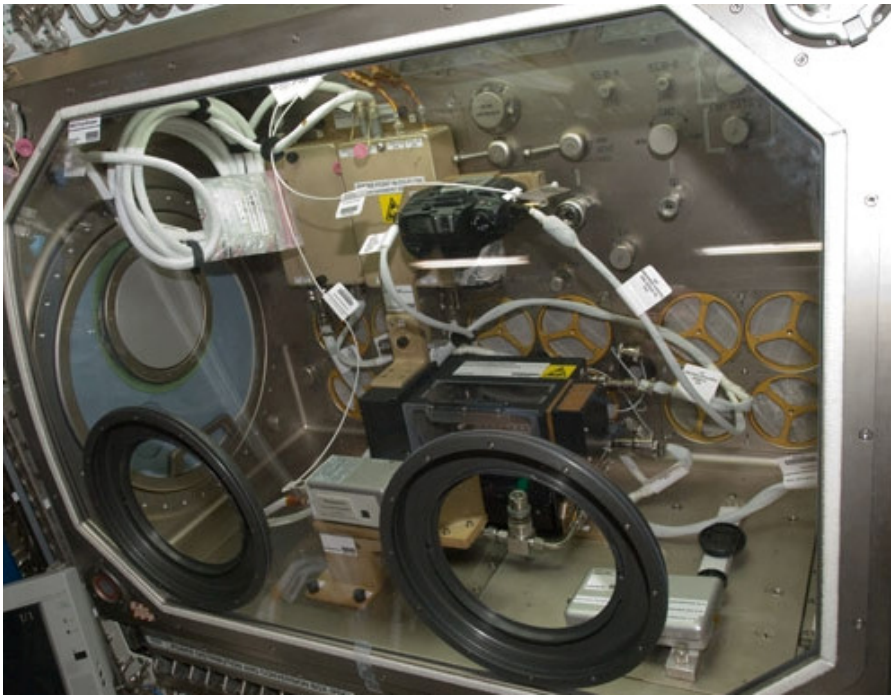

Figure 3.3. SPICE module operating on the ISS in the MSG. SPICE module is the black and gold body at the center, the analog camera is the gray body in front of the SPICE module and the location of the Nikon™ camera is seen as the black object above the SPICE module. Original in color.

3.1.1. Air Metering

As described in the previous section, the velocity of the coflow was measured by an onboard hot-element anemometer. Shown in Figure 3.4 is the correlation between this anemometer reading and another, measuring the air velocity at 13 mm above the tip of the burner tube and aligned with the centerline of the module. This value, obtained much farther downstream of the SPICE module anemometer, was considered more

representative of the coflow velocity within module near the location of the tested flames. This calibration was performed with the burner nozzle in place.

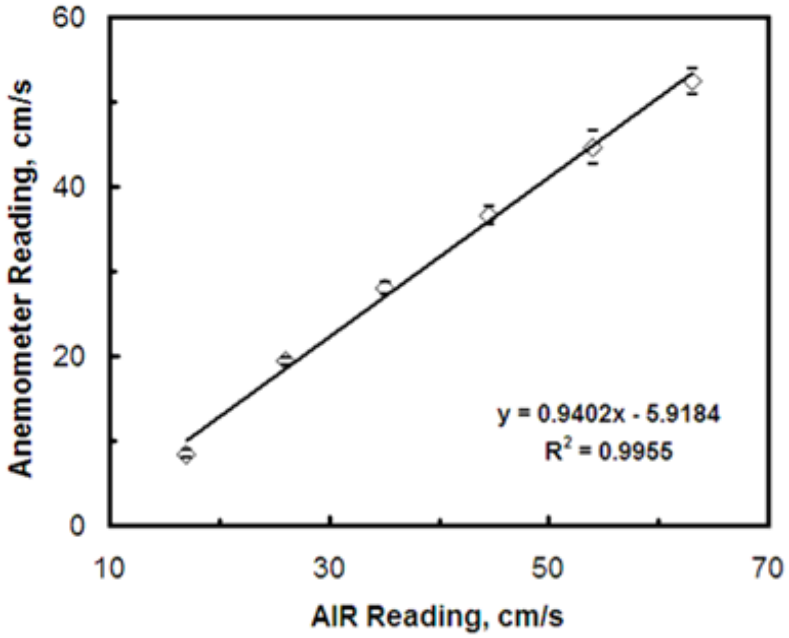

Figure 3.4. Correlation between AIR reading (SPICE anemometer reading on SPICE video overlay) and anemometer reading at a height of 13 mm above burner tip. Maximum variation shown as black bars.

3.1.2. Fuel Metering

The mass flow controller used for SPICE was manufactured by Sierra®. This device reports flow rate in units of volumetric flow in terms if the flowing fluid was nitrogen at 'standard temperature and pressure'. For Sierra® standard temperature and pressure is 21°C and 101.325 kPa. Converting to the actual flow of fuel requires correcting the measured flow by a factor of gas-specific constant *K*, by the following equation

$$Q_f = KQ_{N2}, \tag{3.1}$$

where Q is volumetric flow rate, and subscripts f and $N2$ are for fuel gas and nitrogen, respectively. The constant K for a mixture, $K_{mix,}$ of i components is given by the equation

$$K_{mix} = \frac{1}{\sum_i X_i / K_i}, \tag{3.2}$$

where X_i is the mole fraction of species i. Table 3.2 provides the values of K for the relevant gases in this study.

Table 3.2. *K*-factor for relevant gases.

Gas	N_2	CH_4	C_2H_4	$3C_3H_6$-N_2	C_3H_6-N_2	C_3H_6	C_3H_8
K	1.00	0.72	0.60	0.582	0.481	0.41	0.36

3.1.3. Video and Photography

The images from either the still camera or screen captures from a relevant video file were analyzed in the freeware program, Spotlight™, which was supported by NASA. Reference images of scales were analyzed as well to provide a correlation between number of pixels and dimensions of length. An 'Aoi line profile' was drawn on the axis of the flame. This tool displays the grayscale intensity along the line profile. The position of the maximum rate of change of grayscale intensity is indicated by the arrow in Figure 3.5 and the intensity at this point can be was of the vertical axis. If the maximum rate of change occurs over a range of pixels, the midpoint of this range was used. Alternatively, the endpoints of the line profile can be shortened until only the linear region of maximum rate of change is visible in the intensity chart window. The

mean intensity can be read off the display. The actual location of this point can be found then by dragging the line profile up or down until the end points of the line profile is at the previously determined mean intensity level, shown in Figure 3.6. Then the pixel location of the endpoint can be determined from the status-bar at the bottom of the window.

This approach was also followed to measure the pixel location of markings on scales used in reference images. The location of the mark could be located by a minimum or maximum of grayscale intensity, depending on the coloring of the scale. A linear fit between the particular scale distance and pixel number was determined from the image analysis and used to obtained full-scale dimensions. These can be found in the Appendix.

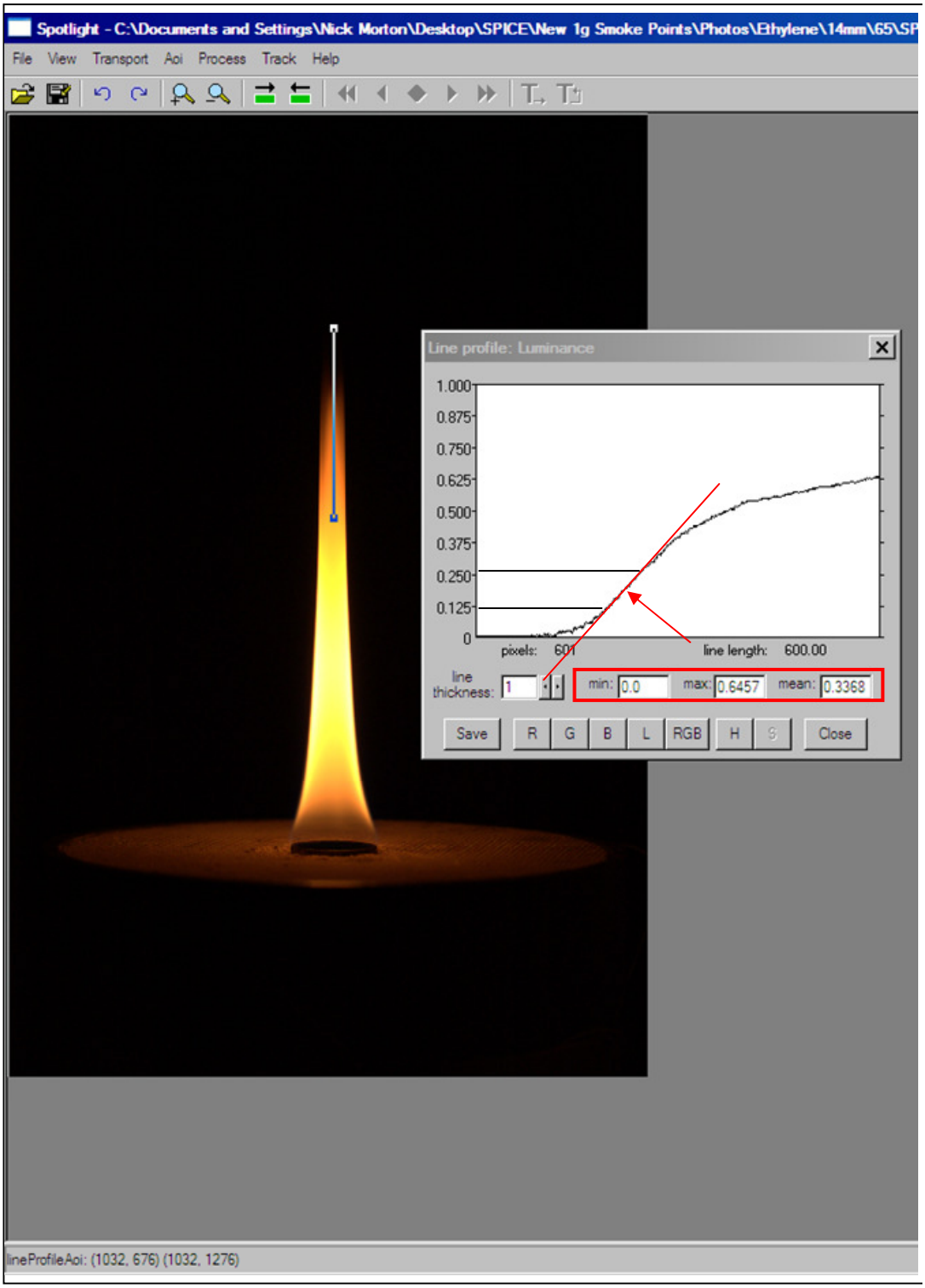

Figure 3.5. Locating the point of maximum rate of change of grayscale intensity. Minimum, maximum, and mean of intensity along the line profile are given in highlighted boxes. Original in color.

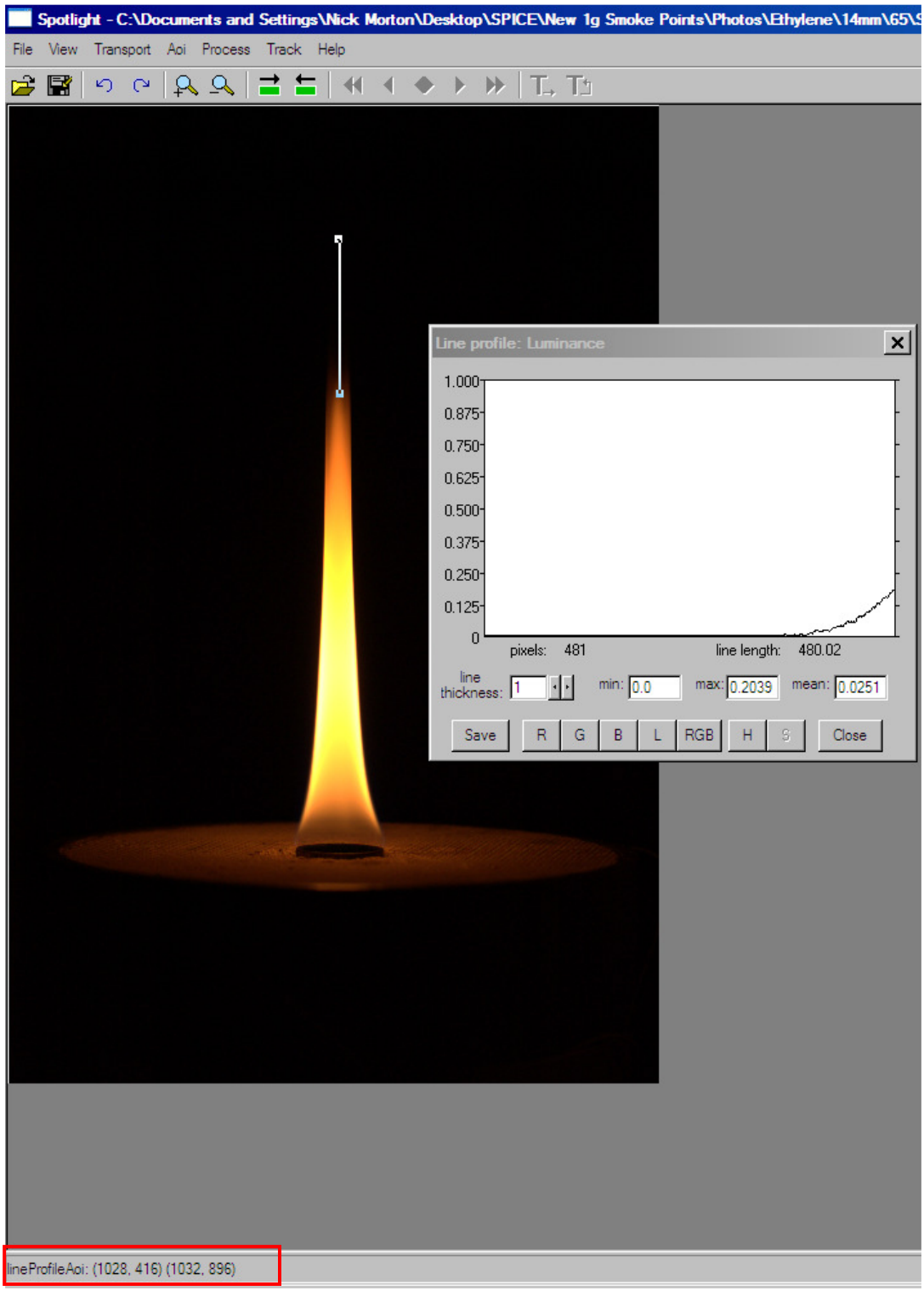

Figure 3.6. Location of flame tip obtained from previously determined value of grayscale intensity. Original in color.

3.2. *SPICE Module on Earth*

Experiments in normal gravity with the SPICE prototype module were conducted at the University of Maryland. The procedure was similar to that on the ISS, however there were slight differences. First, the fuel was supplied though much larger 5.7 and 8.5 kl compressed storage bottles. Second, smoke points were determined visually, not by viewing on a color video display. Third, flame lengths were measured from the still images taken with the Nikon™ color digital camera taken at an f/stop of 5.6 at a -5 EV with +/- 2 exposure bracketing.

The tests were not conducted within a glovebox. Fresh air was constantly available. Combustion product gases and coflow were removed through an exhaust duct, as shown in Figure 3.7. The camera systems are also visible in this figure. Fuel was supply by large fuel bottles supplied by AirGas®. The gas qualities were 99.5% pure for ethylene and propylene, 99.99% pure for methane and 99.0% pure for all others. Smoke point luminous flame lengths were found from the digital still images according to the method presented in Section 2.1.3.

Figure 3.7. SPICE prototype module operating at the University of Maryland FETS Lab. Exhaust and camera systems are visible.

3.3. *Unconfined Coflow Smoke Points*

Smoke points were also found for normal gravity conditions with a much different experimental setup. Tests were conducted with a coflow burner with a 13.7 mm ID burner. Contrary to the earlier tests with the SPICE prototype hardware, this setup did not confine the burner in a cylindrical chimney but rather left it relatively open to the environment.

3.3.1. Coflow Burner

A diagram of the coflow burner is shown in Figure 3.8. Filtered compressed air was flowed in through the air inlet. Its flow was homogenized by glass beads and a

ceramic honeycomb, separated by a fine metal screen. Fuel was routed from the fuel inlet to the fuel nozzle. Sufficient distance was allowed for fully developed pipe flow at the fuel nozzle. The near entirety of the coflow burner was constructed from brass. The fuel nozzle was 13.7 mm ID and 15.8 mm OD. The ID of the coflow cylinder was 101.2 mm.

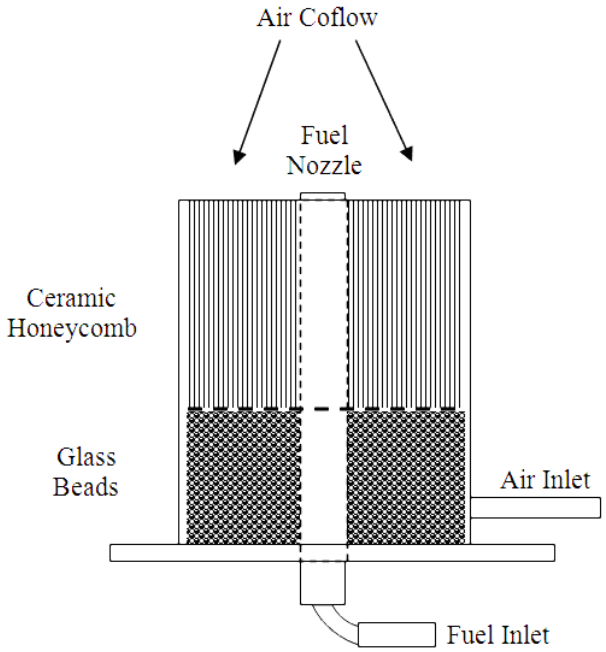

Figure 3.8. Coflow burner for unconfined coflow smoke points. Not to scale.

The coflow burner and flames were protected from exterior flows by cardboard C-channel shroud approximately 0.3 m high, as shown in Figure 3.9. The left face was black and the upper and lower faces shown in the figure were white so that soot could

Figure 3.9. Coflow burner shroud and location of still camera.

be observed. The flame could be observed from looking over the top of the shroud.

3.3.2. Fuel and Air Metering

Fuel was supplied by fuel bottles from AirGas®. For this run of tests only ethylene, propane and propylene were used. The gas qualities were 99.5% pure for ethylene and propylene and 99.0% pure for propane. Fuel volumetric flow was measured with a Gilmont® GF-1260 (glass float) rotameter (accuracy is the greater of 2% of reading or ± 1 scale division). Flow was metered with the use of multiple pressure regulators and a needle valve upstream of the rotameter. Tank pressure was reduced from high pressures in the tank (140 to 3000 psi, depending on fuel) to 60 psig with the tank pressure regulator. The pressure was further reduced to 30 pisg with a pressure regulator just prior to the needle valve. While rotameters are typically dependent on inlet pressure, flow rates were low and inlet pressures were to close to that of ambient pressure.

The rotameter was calibrated for each fuel with the use of a bubble meter. Soap films were formed by the flow of gas within graduated volumetric cylinders. Volumetric flow was determined from timing the travel of the soap film. The fuel gas was assumed to be dry (zero water content) within the fuel tank and at 100% relative humidity once in the bubble meter. The fraction of water vapor present was determined from measurement of the ambient temperature and pressure. The air temperature within the lab was measured with a Fluke® temperature meter with thermocouple probe. From the temperature the vapor pressure of water was

determined from a saturated steam table. Pressure was recorded from the NOAA website for the College Park Airport (http://weather.noaa.gov/weather/current/KCGS.html). This pressure is the mean sea level pressure (MSL, i.e. altimeter pressure). The College Park Airport is at an elevation of only 14.6 meters. The difference in pressure was shown to be negligible by the following process. To obtain an approximation of the actual pressure, the following differential equation was integrated

$$\frac{dp}{dz} = g\frac{Mp}{TR}, \tag{3.3}$$

where p is pressure, z is altitude, g is gravitational acceleration, T is temperature (assumed to be the airport temperature and invariant), M is molecular weight of air, and R is the universal gas constant. The resulting equation is

$$p = p_{MSL}e^{\frac{-gMz}{TR}}, \tag{3.4}$$

with g = 9.81 m/s^2, M = 28.85 g/mol, R =8.314 J/K·mol, and z for the College Park Airport is 14.6304 m. The difference between P and P_{MSL} was shown to be within the 4th significant digit. The final calibration curves can be found in the Appendix.

Two rotameters were used for measurements of the flow rate of the coflowing air. For low flow rates, an Omega® FL-2063-NV was used (quoted range between 20 – 140 lpm of standard air with 3% of full range accuracy). For higher flow rates an

Omega® FL4512 rotameter was used (quoted range between 1.4 - 14.5 cfm of standard air with 2% of full scale accuracy). Air was supplied through the J.M. Patterson Building compressed air system. The air was filtered with a Beach® model F-T20C t-line filter, removing moisture, oil vapor and particulates. Its flow was controlled by a pressure regulator placed at the exit of the filter. A pressure gage measured the inlet pressure at the rotameter.

Volumetric flow rates of air were too high to allow the use of bubble meters. Instead a dry test meter was used to calibrate the air rotameters. A dry test meter (Singer® American Meter Division DTM-115) measures the volume of fluid that has passed through it. By recording the time between volume readings, a volumetric flow rate could be measured. The results of the calibration showed that the true flow rate could be determined by the following empirical relationship

$$Q = Q_{FM}\left(\frac{p_g + p_\infty}{p_\infty}\right)^{1/2}, \tag{3.5}$$

where Q is volumetric flow rate, Q_{FM} is the flow rate reading on the rotameter, p_g is the gage pressure reading at the inlet of the rotameter, and p_∞ is the ambient pressure.

3.3.3. General Procedure

The post-filter pressure regulator would be adjusted to until the air rotameter reading was on a marked flow increment (to reduce reading error). The inlet pressure and reading of the air rotameter were recorded. The fuel tank valve was opened and the

fuel needle valve was adjust until the smoke point condition was reached, determined through a combination of visual analysis techniques, and the fuel rotameter reading was recorded. Digital still photos were taken with a Nikon™ D100 digital color camera with Nikkor™ 50mm f/1.4 AIS lens over a range of f/stops from 1.4 to 16 (ISO 200, shutter speed 1/250 s).

Measurement of the flame length was performed similarly to the previously described sections, with a couple of differences. First the location of the zero datum was estimated to be the center of the visible fuel jet burner as shown in Figure 3.10, and the pixel location of the luminous flame tip (with the previously described method) was found. The total pixel length was determined from by the vector length between these two points. This pixel length was converted to an actual length using the correlations determined from reference images given in the Appendix. Lengths were determined from f/stops 1.4, 2, and 2.8 for each test point.

Figure 3.10. Location of zero datum for flame length

In addition to visual determination of the smoke point, described in the first paragraph of this section, smoke emission was checked for by the insertion of a hydrogen diffusion flame into the downstream combustion products plume of the tested coflow diffusion flame. When the hydrogen flame is properly placed, its luminescence increases from a faint blue (with some red) to a brighter, bluer flame from the excitation of entrained CO_2. Any soot particles present in the products stream will rapidly rise in temperature and release bright blackbody radiation within the hydrogen

flame, indicating soot emission. At times this helped confirm the presence of soot when it was difficult to see by an unaided eye. A properly placed hydrogen flame was more accurate at indicating the presence of small amounts of smoke.

Chapter 4. Results and Discussion

4.1. Microgravity Smoke Points

Smoke points were obtained for five fuels, as summarized in Table 3.1. Smoke points could not be obtained for methane before the flames would impinge on the copper plate at the end of the duct. These flames did not show any signs of approaching their smoke points before impinging on the plate. Also shown in Table 3.1 are the ranges of various parameters for which microgravity smoke points were observed.

Some smoke points, for propane and ethylene in particular, were identified by the onset of gradual dimming and reddening of the luminous flame tip in the downstream direction. Rounding of the flame tip was also associated with the smoke point for these flames. Conversely the brightest flames did not always display significant reddening or darkening near their tips, except when well above the smoke point. This occurred for the pure propylene and propylene mixtures, and the smoke point was identified by the rapid transition to an open-tipped, soot emitting flame. For conditions sufficiently above the smoke point, quenched soot could be seen leaving the flame.

Flames of propylene and propylene mixtures were found to be generally more luminous than those of methane, ethylene, and propane, resulting from their higher propensity to form soot. Periodic flame motion was observed in some flames, especially those with high coflow, long length, and low fuel velocity, and this is

attributed to non-uniform coflow. Propane flames appeared to be especially susceptible. However, this effect was small and did not prevent clear measurement of the flame length. For ethylene and 1.6 mm burner propane flames, the smoke point transition was not surpassed to a large degree so there is some uncertainty whether these points are smoke points, or that the actual point could be slightly higher.

The present smoke points were found to be repeatable, except for propylene with the 0.41 mm burner. Testing on different days yielded different smoke points for this combination. This is attributed to a change in the duct exit system, which became partially clogged with soot and required higher fan voltages to obtain a given coflow air velocity reading. The lower smoke points were obtained with a relatively clogged exit, and the highest smoke point was found after the exit was vacuumed clean. For all of these tests, the air coflow rate was set based on the hot-wire anemometer velocity reading. The flow restriction in the exit may have altered the coflow in some manner and also the measured smoke points. Other smoke points collected on these two dates did not exhibit this same discrepancy so this coflow quality effect may only affect flames of this smallest burner diameter. It could be surmised that the coflow is less uniform for the case of higher fan voltage for a particular flow rate.

Figure 4.1 shows images for representative flames near their smoke points. Two sequences are shown, and in both the smoke point occurs between the third and fourth flames. In the top sequence, coflow velocity decreases from left to right at a constant fuel flow rate. This increases luminous flame length and reduces the smoke point,

leading to soot emission. The luminous length decreases in the fourth image because it was taken at a shorter shutter time. In the bottom sequence fuel flow rate is increased at a constant coflow velocity, increasing flame length as expected. As seen in Figure 4.1, luminous length is more sensitive to changes in fuel flow rate than to changes in coflow velocity.

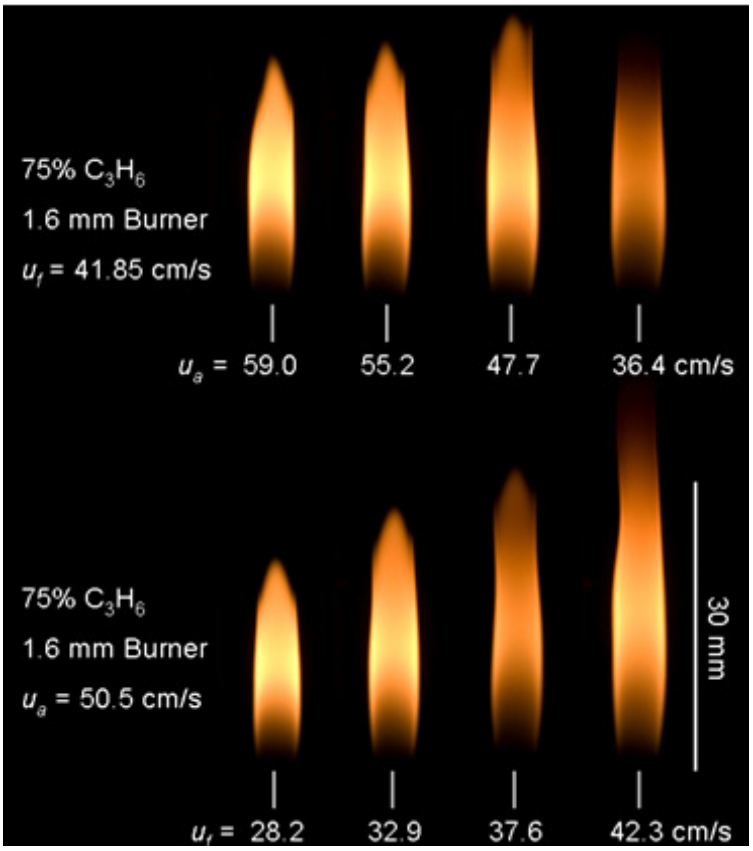

Figure 4.1. Color still camera images of 75% C_3H_6 flames with (top) decreasing coflow velocity at a constant fuel flow rate, and (bottom) increasing fuel flow rate at a constant coflow velocity. Images were taken at f/11 with a shutter speed of 3.1 ms (except the 4th top and 3rd bottom pictures, which involved a shutter speed of 1.3 ms).

In Figure 4.2 the measured smoke point lengths are plotted with respect to coflow velocity. For a given choice of fuel and burner diameter, an increase in coflow velocity generally increases the smoke point length. This behavior could be attributed

to decreased residence times in the soot formation region as the coflow velocity is increased. Alternatively, if soot oxidation in the post-flame-sheet region is limited by oxidizer transport into the region, then increases in coflow velocities would increase the rate of soot oxidation. This would delay the smoke point transition to higher fuel flow rates until the rate of soot formation overcomes the rate of soot oxidation. The variation of smoke point with coflow velocity is greater for longer flames, than for shorter flames. However, this cannot be described by some length effect because that would have led to a nonlinear response of smoke point to coflow velocity.

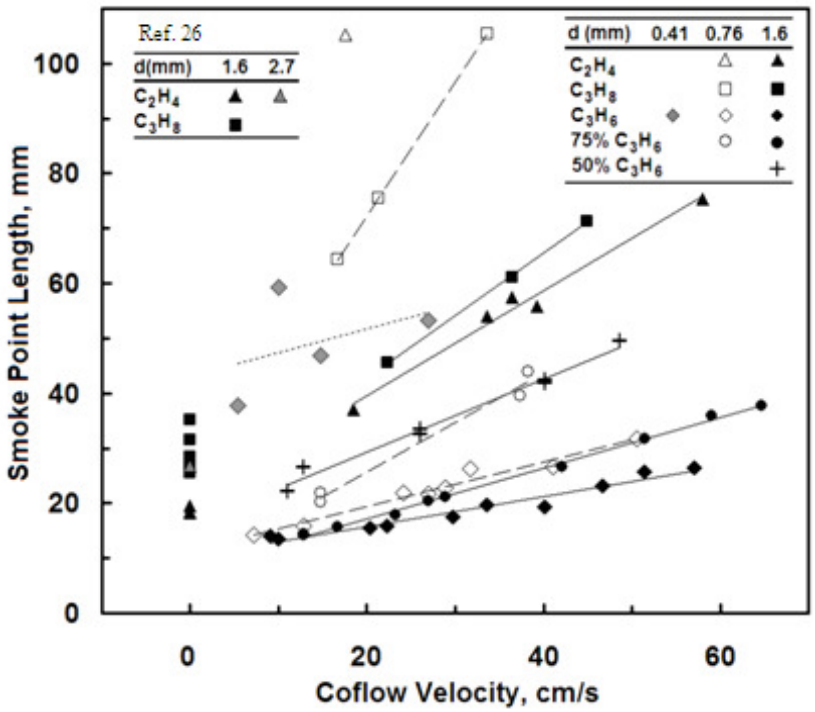

Figure 4.2. Smoke point luminous flame length plotted with respect to coflow velocity. The lines shown are fits for each pairing of fuel and burner diameter for the present data.

Figure 4.2 reveals that smoke points of nonbuoyant coflow flames increase with decreasing burning diameter. Kent and Wagner's work[25] suggested that this finding would result as increased fuel jet exit velocities shifted the centerline soot volume

fraction profile downstream and this may therefore reduce the soot formation time. The larger jet exit velocities should also reduce soot formation time as flame length depends most strongly on mass flow rate of fuel, not velocity. It was observed the still images that flames with higher initial velocities had a notable soot-free zone immediately after the jet exit.

The difference in smoke point between 1.6 and 0.76 mm burners is not as strong as the difference between 0.76 and 0.41 mm. This would indicate that the effect is nonlinear or depends on interactive effects with other controlling parameters. The effect of fuel dilution can also be seen, with an increase in smoke point flame length with increasing the N_2 content of propylene. Note that the smoke points for pure propylene with the 0.76 mm burner are close to the values of the smoke points for 75% propylene with the 1.6 mm burner. Also the smoke points for 75% propylene with the 0.76 mm burner are close to that of 50% propylene with the 1.6 mm burner. While the mechanism is not necessarily the same, the smoke point displays a similar response to diameter decreases and fuel dilution increases.

As increasing the fuel dilution increases the fuel jet exit velocity at a particular mass flow rate of hydrocarbon fuel, this raises the question of whether dilution increases the smoke point by reducing the flame temperature, diluting the soot concentration, or increasing the fuel jet exit velocity. Table 3.1 indicates that there are only minor changes to the adiabatic flame temperature. Figure 4.3 shows that the fuel jet exit velocity at the smoke point condition for the diluted propylene smoke points is not as

large as it is for the smaller diameter propylene smoke points. It would follow that fuel jet exit velocity is not the only factor increasing the smoke point for the diluted fuels and that the diluting effect in of itself is driving this change as well.

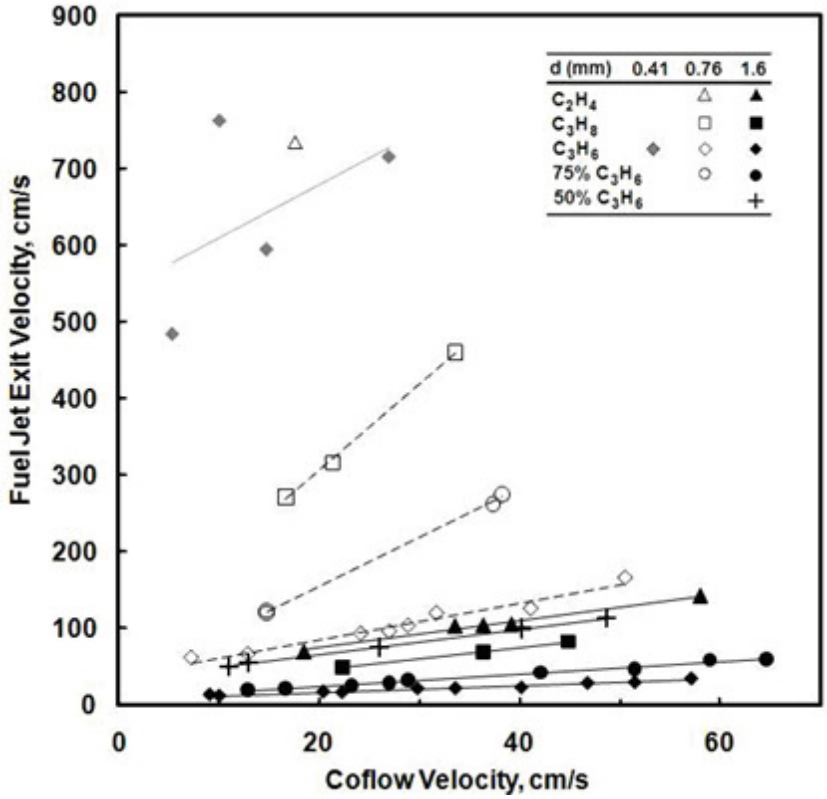

Figure 4.3. Fuel jet exit velocity at the smoke point plotted with respect to coflow velocity.

This burner diameter dependence differs from previous observations of microgravity flames in still air,[38,39] whose smoke points were only weakly dependent on burner diameter. These points are also shown in Figure 4.2 at zero coflow velocity. SPICE and still air data for propane and ethylene are shown in Figure 4.4. Linear fits the combination of the data yield high R^2-values (greater than 0.95). For propane the combination of the 0.76 mm burner and the still air data has a slightly higher R^2-

value, indication a better fit. It is likely that smoke points in the linear region between these two data sets would be found in roughly the area indicated by the linear fits.

The sooting propensity of the present fuels, identified from in the smoke point length for the 1.6 mm burner diameter and fixed coflow velocity, is generally propane < ethylene < 50% propylene < 75% propylene < propylene. This is consistent with what is found for typical normal gravity smoke points in coflow. An exceptional case was observed for the 0.76 mm burner. Ethylene had a longer smoke point length than propane. This could be a result of residence time effects associated with the lower

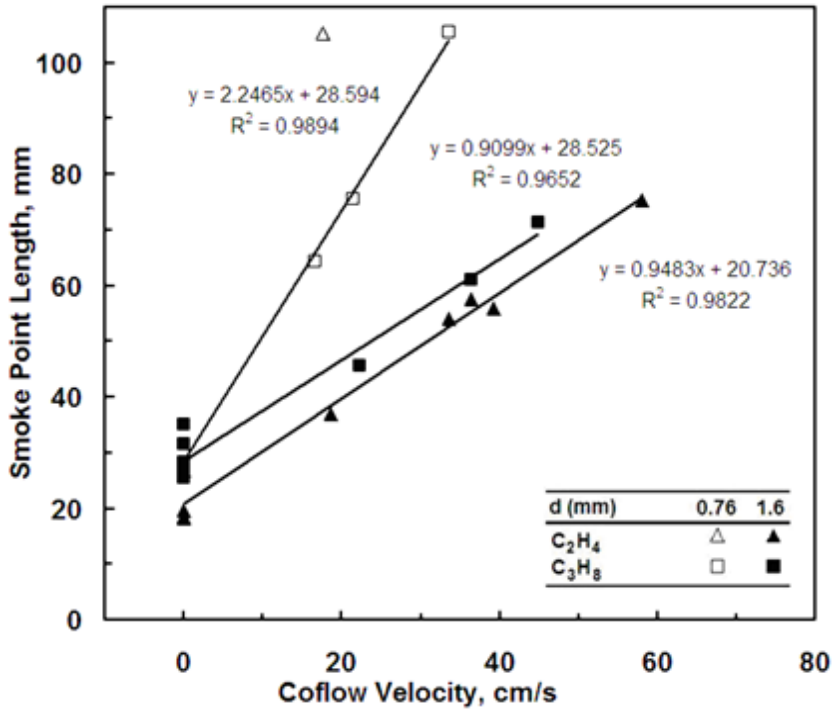

Figure 4.4. SPICE data correlation including zero coflow data from Urban et. al.

density ethylene having a much large exit velocity at an equivalent mass flow rate of fuel.

In Figure 4.5 the smoke point flame lengths are plotted with respect to $\dot{m}_f / Z_{st}$. This is motivated by Eq. (2.11). This choice of axes yields a reasonably good single correlation of the luminous lengths of all fuels. Although this plot is for conditions at the smoke point, data for flames at not at their smoke points are expected to generally follow this correlation. This correlation, however, does not account for the decrease of flame length with increased coflow velocity (see Figure 4.1). These results are similar to those of Lin and Faeth[42] in that the proportionality between L_{SP} and $\dot{m}_f / Z_{st}$ increases for flames with low $u_{a,o} / u_{f,o}$ velocity ratios. This effect on lengths is observed for propylene, propane, and ethylene flames with the smallest burners, for which $u_{a,o} / u_{f,o} < 0.08$.

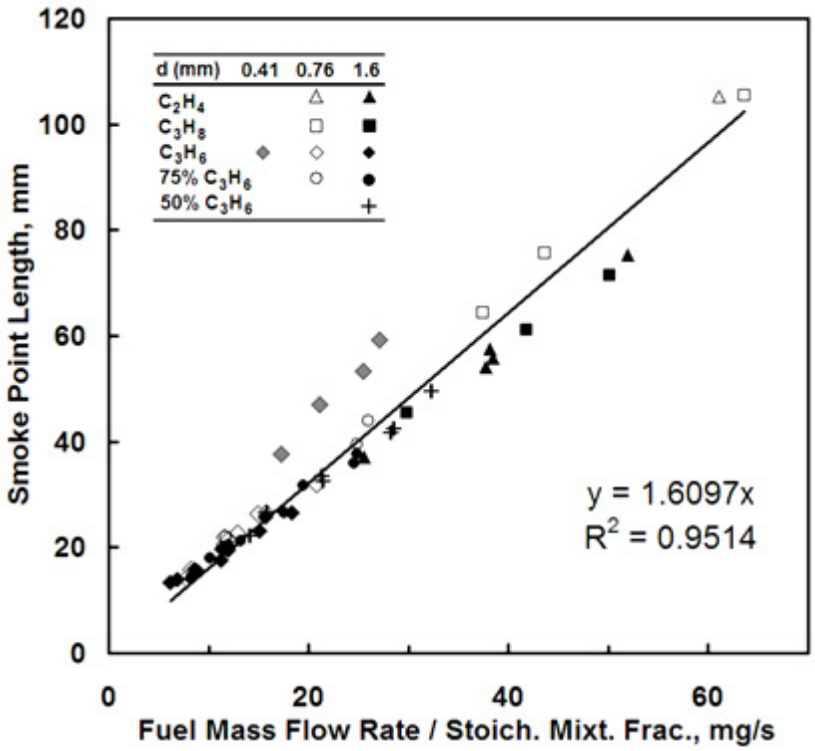

Figure 4.5. Smoke point luminous flame length plotted with respect to fuel mass flow rate divided by stoichiometric mixture fraction. A linear fit that intersects the origin is shown.

This factor is not present in the luminous flame length equation for the coflowing case given in Equation (2.10), because radial velocity was neglected and the axial velocity is assumed to be constantly and uniformly that of the surrounding coflow. This assumption is only justified far from the fuel jet exit, where the axial velocity could be assumed to be uniformly the coflow velocity, or when air and fuel velocities are matched. This secondary flame shape effect likely manifests from the deficiency of this assumption regions near the jet exit. Strong fuel jets in a weak coflow are likely to be better approximated by Equation (2.5) for the still air case.

One can further support this assumption with the following plots. Adding in data from the Laminar Soot Processes (LSP) experiment for microgravity flames in still air and correcting the SPICE and LSP data by a virtual origin correction factor produces Figure 4.6. Here the virtual origin for LSP is -5.9 mm as obtained from a linear correlation of L_{SP} versus $\dot{m}_f / Z_{st}$ for the propane data, and the virtual origin for SPICE is 4.0 mm as obtained from a linear correlation of all the 1.6 mm data and including propylene data for 0.76 mm burner, which all have relatively low initial air to fuel velocity ratios. The slope of the gray points (LSP and 0.41 mm propylene, neglecting possible outlier point indicated in the figure) is approximately 1.44 times the slope of the 1.6 mm burner points. It could be concluded that flames with high initial fuel velocities relative to the surround coflow would better correlate with the length correlation predicted by Equation (2.5) for flames in air still.

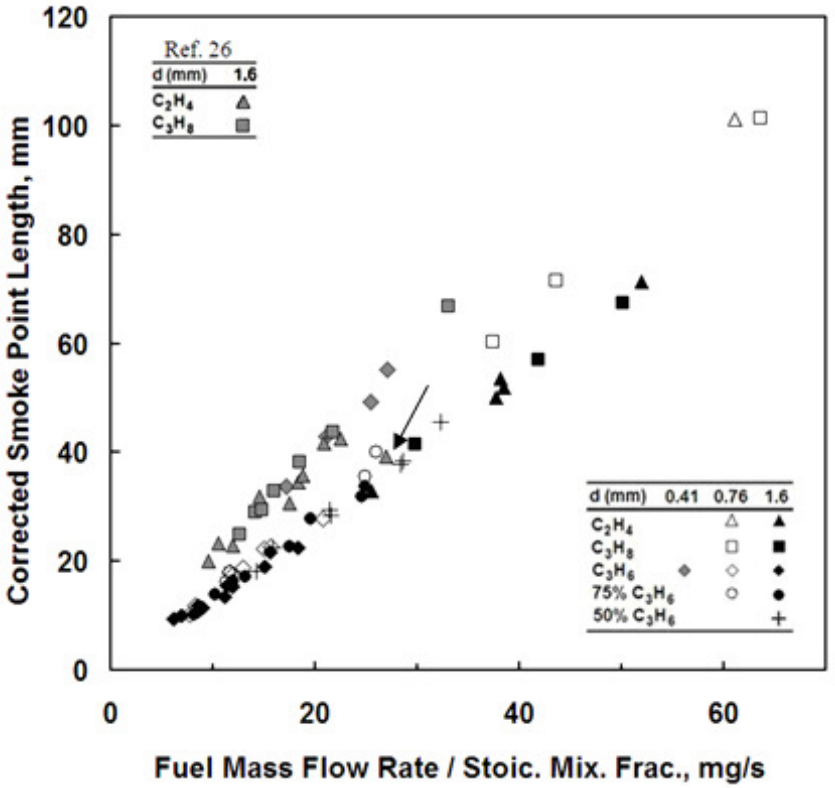

Figure 4.6. Smoke point luminous flame lengths corrected by virtual origin. Arrow indicates possible outlier in LSP data.

4.2. Normal Gravity Smoke Points

4.2.1. SPICE Module

Similar results were found for normal gravity smoke points obtained with the prototype SPICE module, which was essentially identical to the equipment used for the tests on the ISS. The flames were similar in appearance to the microgravity flames. An additional difficulty encountered while searching for smoke points was that the flames tended to lift at lower fuel and/or coflow velocities, and the smoke points occurred at longer luminous flame lengths, when compared to the microgravity

results. As a result fewer smoke points were found. Also fewer smoke point tests were performed in general.

Figure 4.7 shows the coflow dependence of the smoke point for these normal gravity flames. Contrary to what was seen for the microgravity tests, there is not significant variation in the rate of change of the smoke point with coflow velocity. This may, however, be due to the smaller range of flame lengths tested. There appears to be strong diameter dependence. There is a larger change in the smoke point of propylene with decreasing diameter on an absolute and relative scale as compared with the microgravity results. Sooting propensity is similar to the microgravity results and to what has been consistently shown in the literature, that increasing inert concentrations

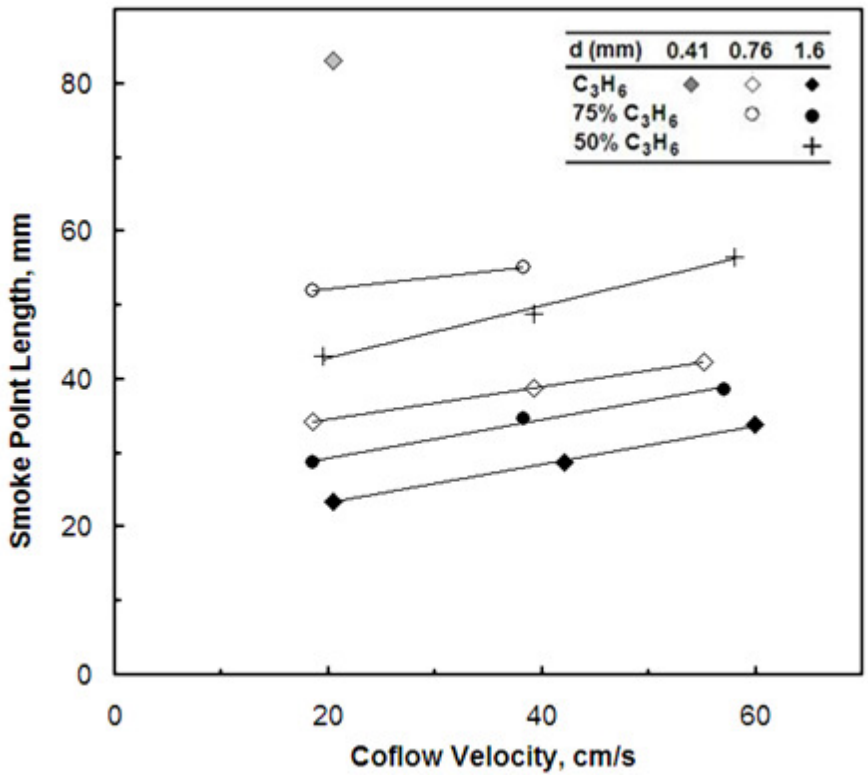

Figure 4.7. Variation of normal gravity smoke point with coflow velocity for normal gravity flames obtained with the SPICE module.

increase the smoke point.

Smoke point flame length correlates with fuel mass flow over the stoichiometric mixture fraction, as shown in Figure 4.8. Variance in the data is smaller than for the microgravity smoke points. While the 0.76 mm 75% propylene flames appear to be slightly higher than the correlation, the difference is not great. However, the smoke point found for propylene with the smallest burner diameter is significantly longer

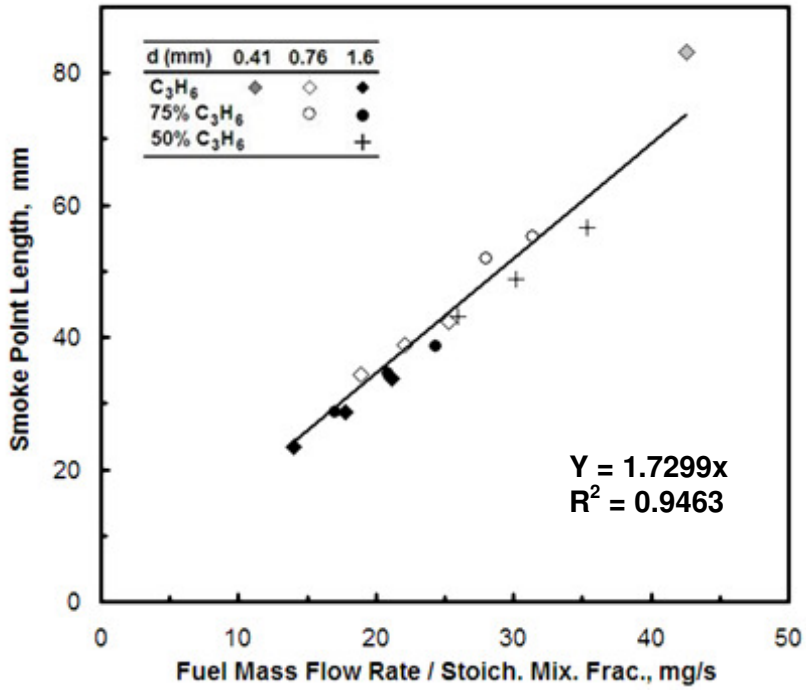

Figure 4.8. Normal gravity smoke point luminous flame length plotted with respect to fuel mass flow over stroichiometric mixture fraction. Linear fit forced to intersect the origin is also shown.

than what would be predicted by a linear fit of the data, forced to intersect the origin or not. This could be a similar velocity ratio effect as seen for the microgravity smoke point flame lengths. Although it is a single point, considering the results of the previous section and the possibility of collecting a long flame length in error is

unlikely (such a flame would be heavily smoking), it is possible that this flame is longer than expected owing to its much larger jet exit velocity relative to the other collected smoke point flames.

4.2.2. Unconfined Coflow Burner

Three different fuels were tested with the unconfined coflow burner: propane, ethylene, and propylene. Ethylene and propylene appeared laminar and flicker-free over a range of coflow velocities. Propane on the other hand appeared to exhibit flame instability near its tip for all test points, increasing with fuel flow rate. The instability was not in the form of flickering. Beginning near the flame tip, oscillating waves began travelling along the vertical axis of the flame. This could be an indication of the onset of turbulent behavior or the sign that the coflow velocity was beginning to decay to the detriment of flame stability. Propane flames were the longest of any tested flame; therefore both factors are likely contributors.

It is worth noting the experimental limitations encountered in acquiring smoke points. For propane significant flame flickering occurred at coflow velocities below the range shown in Figure 4.9. Above the shown range the flame began to detach from the burner nozzle. This was not a lifting phenomenon as seen in with the SPICE module tests but parts of the flame base would disappear in sections or slices. Obtaining smoke point flames was not attempted when this occurred. The lower bound for ethylene was also determined by the point flame flickering subsided. However the upper bound for coflow velocity was determined by the point at which the flame

would emit soot at all flame lengths. The lower bound of coflow velocity for propylene was limited by the range of the air coflow rotameters and the upper bound was conversely limited by the range of the fuel gas rotameter. It both cases the readings were taken at the lowest end of the respective rotameter scales.

The smoke points found for the unconfined coflow burner displayed different behavior. As shown in Figure 4.9, propane smoke points continued to increase in length with increasing coflow velocity while smoke points for ethylene and propylene decreased. The fuel stream is significantly retarded with this configuration, with initial air to fuel velocity ratios ranging between 2.6 - 70. Given that the coflow velocity is likely to decay with distance, it is doubtful that these numbers are

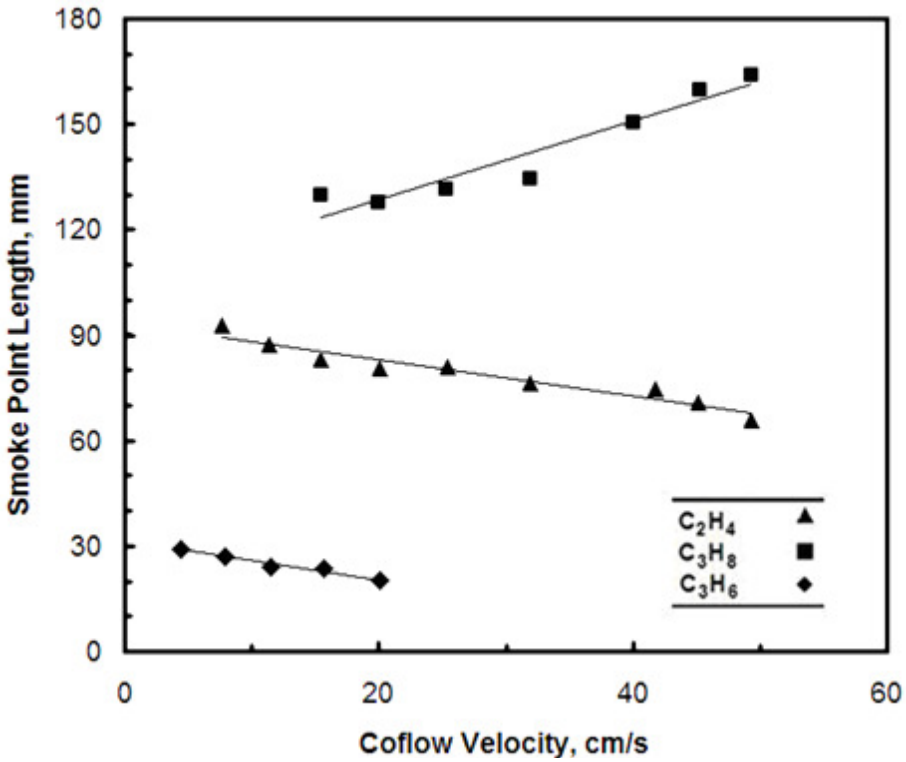

Figure 4.9. Variation of smoke point length with increase in coflow velocity for unconfined coflow burner flames.

representative of the velocity ratios experienced over the entire length of the flame. This may be why the much longer propane smoke point flames continue to increase in length with coflow velocity. The opposite is true for the very short propylene flames; the coflow velocity is unlikely to have decayed significantly near the burner centerline. Air to fuel velocity ratios are highest for propylene, which may indicate that the very rapid coflow is somehow hindering soot oxidation or encouraging soot formation.

Once again consider the results of Schalla and McDonald.[34] Their work (with a 9 mm burner) showed that increases in coflow velocity would cease to increase the smoke point above a particular flow rate of oxidant. This could be interpreted as a transition from a transport-limited regime for soot oxidation to a kinetics-limited regime. It would then follow that for the substantially higher flow rates in the present results that a decrease in smoke point would be caused by a decrease in residence time within the soot oxidation region of the flame. Alternatively this could be explained by some kind of cooling effect in the soot oxidizing region. That is by introducing far more air than what is required to oxidize the soot. Additional experimentation would be required to verify either of these hypotheses.

Figure 4.10 shows that despite the buoyant nature of these flames, their flame lengths correlate with mass flow rate. There is noticeable variance in the propylene data and this is believed to be due to the fuel flow rates measured at the bottom end of the rotameter. The manufacture recommends taking flow measurements near the upper

67% of the rotameter scale for best accuracy. It was also noted that the rotameter bead oscillated more significantly near the lower end of its scale.

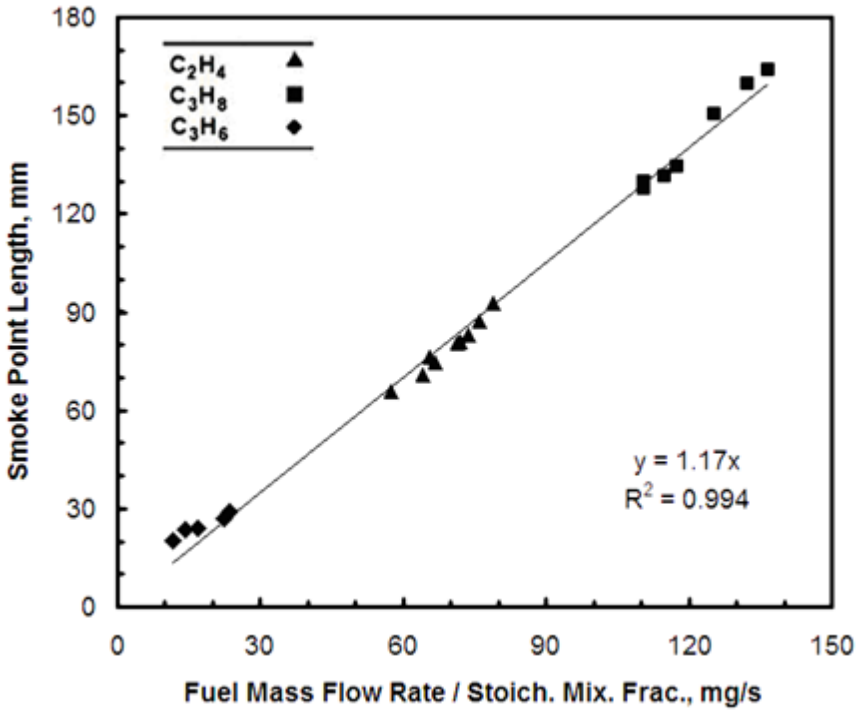

Figure 4.10. Smoke point length plotted against fuel mass flow rate over stoichiometric mixture fraction. A linear fit, forced to intersect the origin, is shown also.

The normal gravity SPICE data can be added to Figure 4.10 to create Figure 4.11. The flame length correlations for these two different test setups differ. This could be related to the whether the coflow is confined, and therefore decelerating or accelerating with distance, or more likely, related to the difference in buoyancy effects. The Froude number is typically cited as a measure of whether a flow is characteristically dominated by buoyant forces ($Fr << 1$) or by its momentum ($Fr >> 1$). It is given by

$$Fr = \frac{u^2}{2gL}, \tag{4.1}$$

where, for a coflow flame system, u can be the air or fuel stream velocity and L is the flame length. For this case of whether coflow of jet exit velocity dominates is not immediately obvious, so an approximate Froude number that is the average of the coflow and jet-exit Froude numbers will be used. For the SPICE normal gravity tests, the average Froude numbers range from 0.1 - 43, indicating that they are transitional to momentum-dominated flows. For the unconfined flows, this Froude number is more than an order of magnitude below 0.1, indicating that these flows are buoyancy dominated. Future work utilizing flame length equations that are proper for buoyant flows would bear whether this is the determining factor causing this difference in

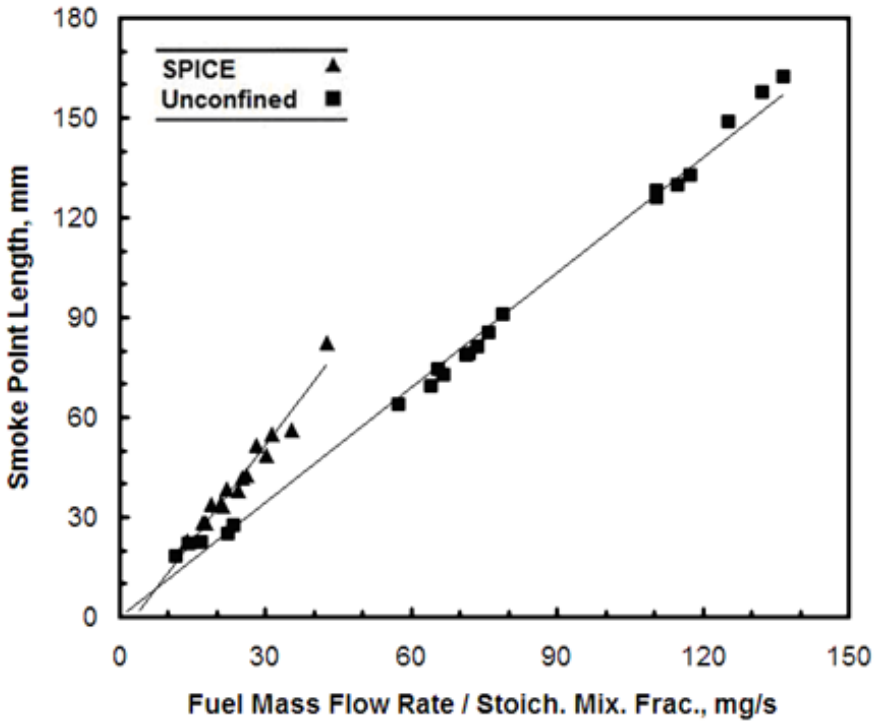

Figure 4.11. Virtual origin corrected smoke point flame lengths plotted against fuel mass flow over stoichiometric mixture fraction for both normal gravity smoke point tests. Linear fits shown also for purely aesthetic reasons. Virtual origins are 0.5 and 1.88 for SPICE and unconfined smoke points, respectively.

slope.

Smoke point data from Schalla and McDonald,[34] Berry-Yelverton and Roberts,[40] and the current study can be combined to form Figure 4.12. It would appear from the figure that the relationship between burner diameter and coflow velocity and the smoke point are not mutually independent. Data obtained from different burner diameters show different behaviors over similar ranges of coflow velocity. A simple non-dimensionalization procedure to collapse the data from these difference sources was not found. Experimental differences, including confinement and Froude number, could be confounding the shown behavior.

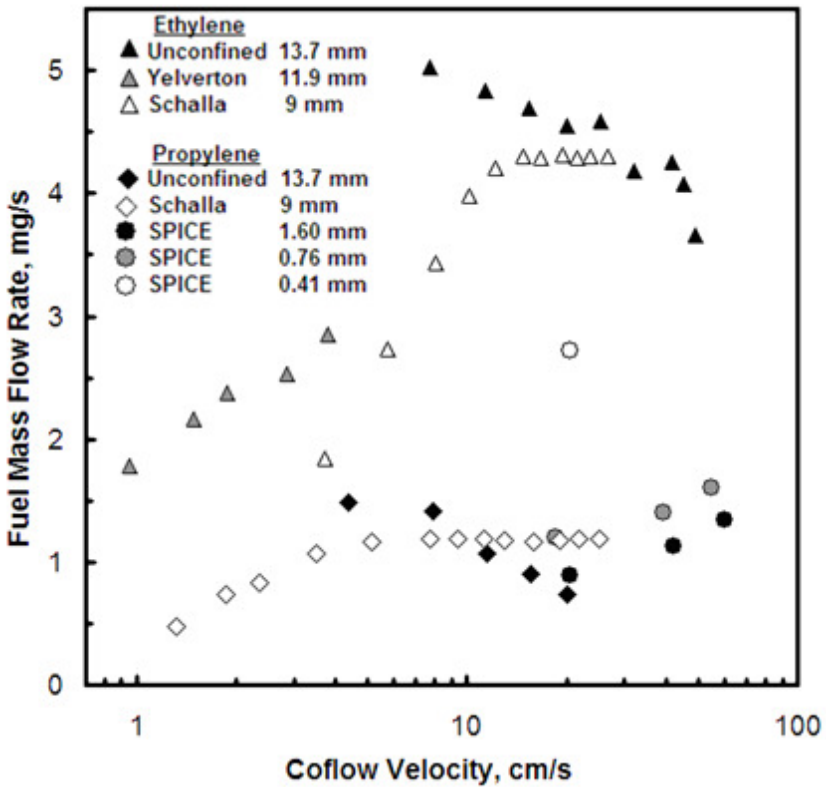

Figure 4.12. Fuel mass flow at smoke point condition versus coflow velocity. Normal gravity smoke point data from a variety of sources.

4.3. *Smoke Point Scaling and COMSOL Results*

Applying Equation (2.23) to the SPICE microgravity flames results in Figure 4.13. The density was assumed to be that of the fuel at 294 K and 101.3 kPa, and the dynamic viscosity was assumed to be that of air at 1500 K. Note that this analysis neglects the influence of combustion related heating on the flow velocities. Although buoyant effects are not present for microgravity flames, expansion is. Overall the simplified analysis predicts that longer smoke points, achieved by increasing the coflow velocity, have lower overall residence times. Also smoke points obtained with smaller burner diameters have shorter residence times. There is no simple relationship, however, between smoke point length and residence time for the various

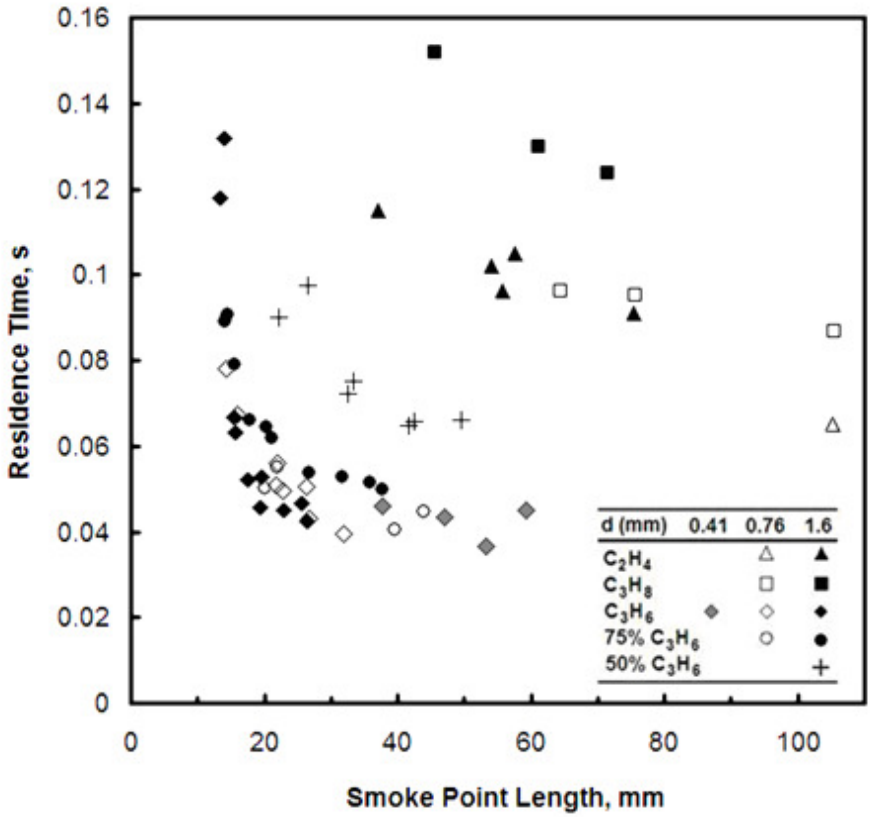

Figure 4.13. Flame residence time for SPICE microgravity smoke points estimated with simplified Schlichting predication for nonreacting jets in coflow.

fuels and burner diameters. It appears that all the propylene-based data, except for 50% propylene, collapse to a single curve.

An estimate of soot formation time can be determined as the time required to traverse the first half of the flame. This is based on the finding that the stoichiometric flame length is about half of the luminous flame length at the smoke point. Soot oxidation time can be estimated as the remaining residence time within the flame. Although soot formation does not start until flame temperatures are sufficiently high, and soot oxidation also occurs in the fuel-rich region of a diffusion flame, this can be utilized as a first approximation. The results are shown in Figure 4.14. Overall a trend of increasing residence time ratio for longer smoke points is shown. A large number of

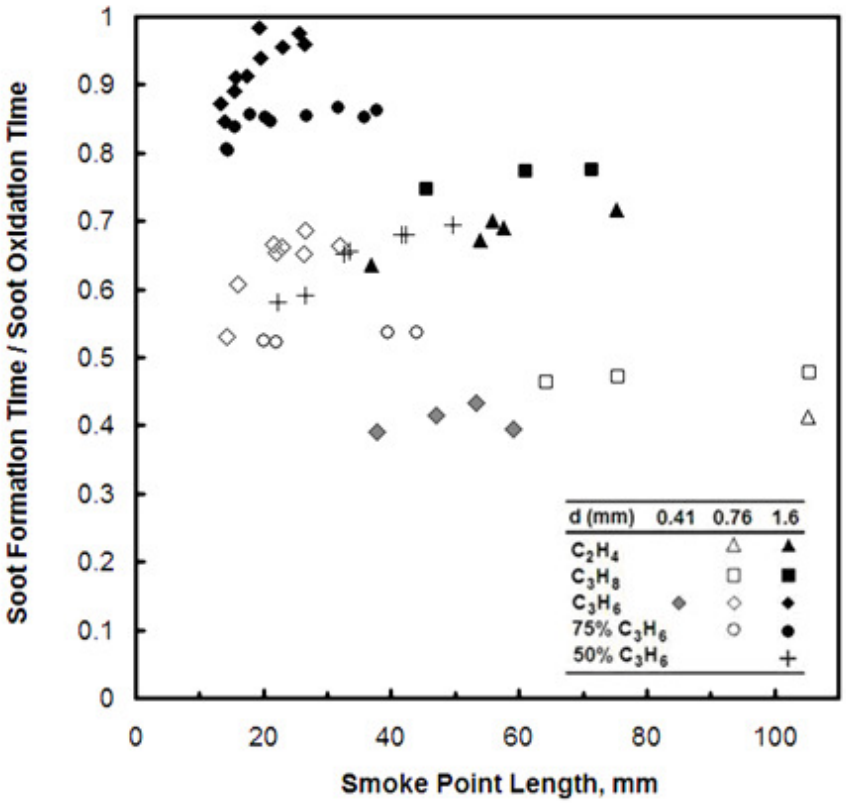

Figure 4.14. Ratio of estimated soot formation time to soot oxidation time (residence time ratio) for SPICE microgravity flames.

the smoke points group around a residence time ratio of 0.65. Pure and 75% propylene for the 1.60 mm burner are significantly higher. These points have high air to fuel velocity ratios. Propylene with the 0.41 mm burner, and propane and ethylene with the 0.76 mm burner are significantly lower, and are points with very low air to fuel velocity ratios. There is not an obvious criticality or specific residence time ratio for these smoke points.

To better evaluate the results of Figure 4.14, consider the results of the following COMSOL® simulations shown in Figure 4.15. Simulations were run on air jets in an air coflow. Tests were run including burner geometry (Numerical) and without burner geometry (Numerical 2). Then the simplified Schlichting analysis was applied (Analytical). Results are shown for comparison purposes for coflow velocities of 0, 5, 10, 25, 50, and 100 cm/s. It is seen that up to 10 and 25 cm/s of coflow velocity for Numerical and Numerical 2, respectively, the analytical prediction matches the simulation data quite well. At some higher velocity, the prediction does not account fully for the initial jet decay. Above approximately 25 cm/s of coflow, the centerline velocity decays below the coflow velocity and then accelerates. Even when the coflow velocity is the same as the initial centerline jet velocity (100 cm/s), there is an initial velocity decay region. This initial decay is stronger when the burner geometry is present.

As shown in Figure 4.16, a boundary layer forms around the burner (shown as white). This occurs because slip is not allowed at the burner surface This low velocity

boundary layer or wake surrounds the jet in the immediate vicinity of the jet exit, shielding the jet from the coflow and enhancing jet velocity decay. This effect is still present in the simulations without the burner geometry for relatively strong coflows because of the initial parabolic profile of the fuel jet. In this case, a low velocity region is still present between the jet centerline and the surrounding coflow and shields the centerline from the effects of the surrounding coflow for some distance downstream from the jet exit. It is likely that an initially uniform jet velocity profile (plug flow) would match the simplified Schlichting prediction much closer than a fully developed jet.

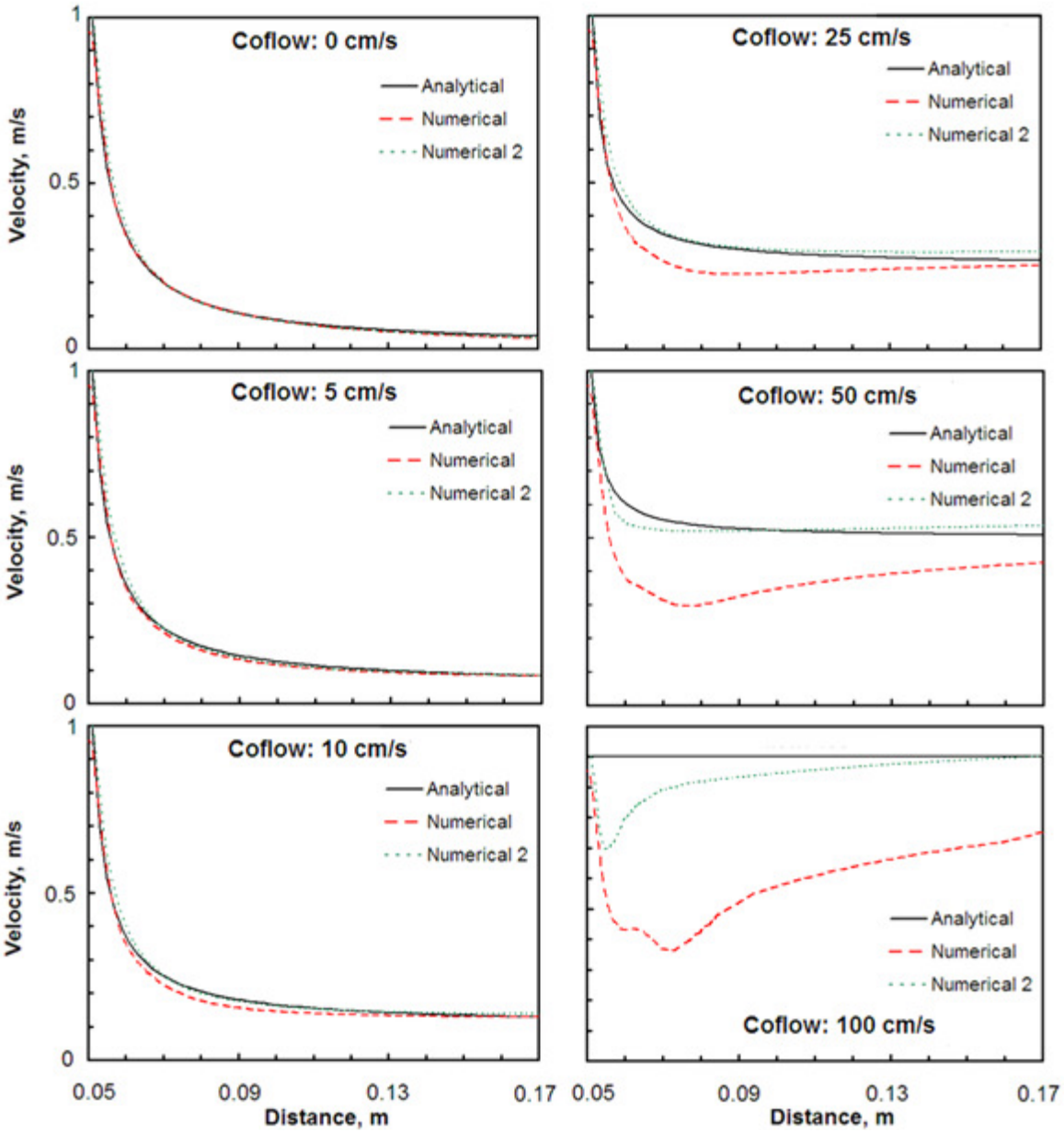

Figure 4.15. Centerline velocity decay of 50 cm/s (mean velocity) air jet in a uniform air coflow of various velocities.

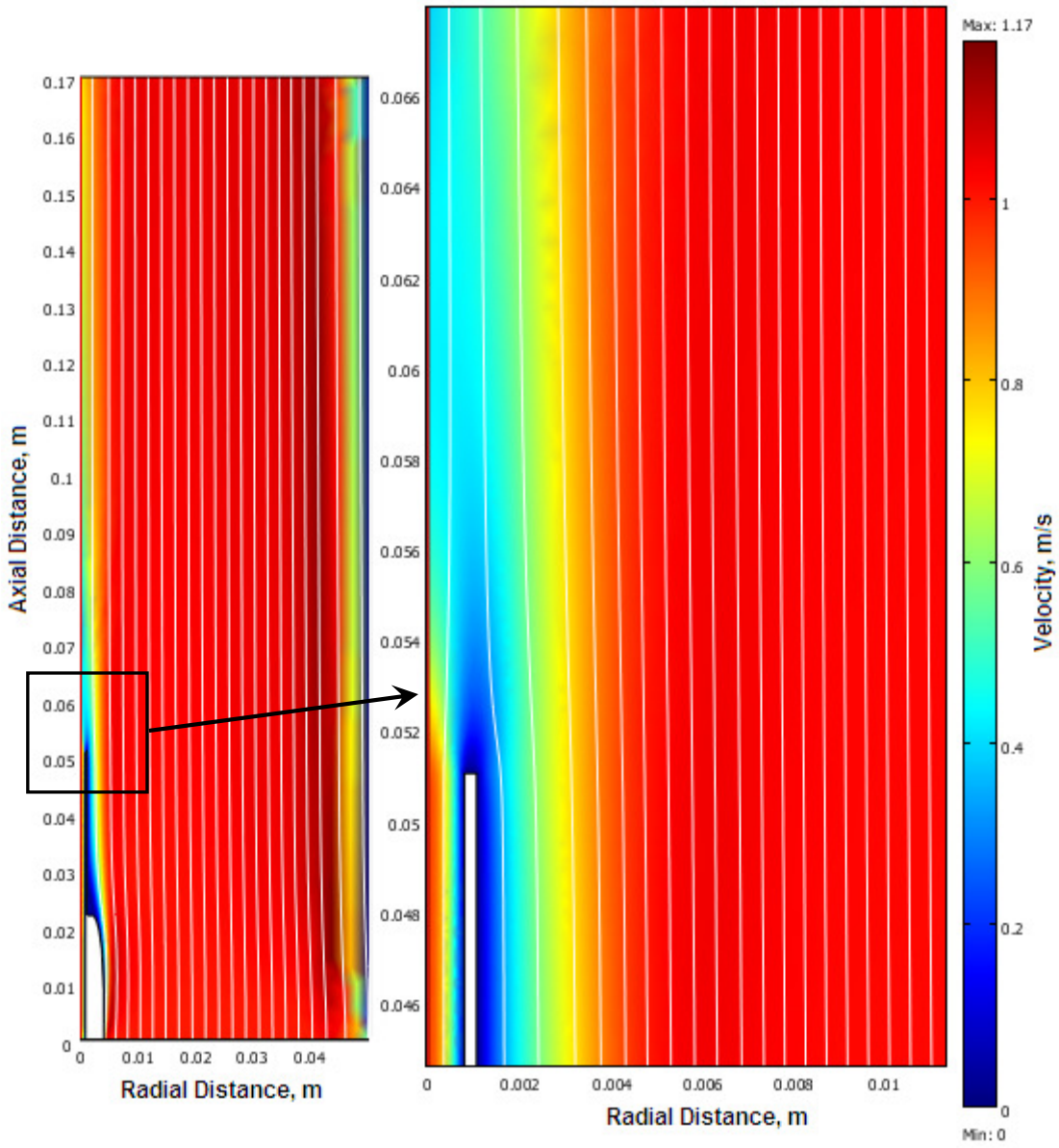

Figure 4.16. Velocity contour map for COMSOL simulation of 50 cm/s mean velocity jet in a 100 cm/s uniform coflow. Burner geometry has been included and is shown in white in the flow field. The entire flow field is shown on the left and a close-up of the flow field near the jet exit is shown on the right.

Chapter 5. Conclusions

Smoke points of microgravity and normal gravity gas-jet diffusion flames were observed. Microgravity conditions emphasized small burners and effects of coflow velocity. These flames allow extensive control of residence time, which may be important in smoke point phenomena. An increase in coflow velocity increases the smoke point length. A decrease in burner diameter increases the smoke point length. These two effects can be explained qualitatively by considering residence times; increased fuel and/or coflow velocities yield increased smoke point lengths. The effect of coflow velocity could also be explained by increased O_2 transport if soot oxidation downstream of the flame sheet is transport limited.

The fuel sooting propensities in these flames are as follows: propane < ethylene < 50% propylene < 75% propylene < propylene, however ethylene is less sooty than propane for the 0.76 mm burner. To the first order, luminous length at the smoke point is proportional to fuel mass flow rate, consistent with past theory and experiments. A second-order effect is that this length increases for low $u_{a,o} / u_{f,o}$ velocity ratios. Flames of this nature approximate the behavior of a jet flame in still air.

Smoke points of normal gravity gas-jet diffusion flames were also observed. For the smaller burner tests in a confined coflow environment, smoke point length increased with an increase in coflow velocity or a decrease in nozzle diameter. For a very large burner in an unconfined coflow, the smoke point length decreased with increasing

coflow velocity for propylene and ethylene, but increased for propane. This, and results of a previous study showing domains where the smoke point is invariant to changes in coflow velocity, indicate that the relationship of smoke point to coflow velocity and nozzle diameter is more complicated than initially expected. It has been hypothesized that the different responses may be due to different soot oxidation regimes, transport-limited, kinetics-limited, and residence-time-limited.

Simplified analysis of the residence time and soot formation time to soot oxidation time ratio of the SPICE microgravity flames failed to yield substantial collapse of the smoke point data or a residence time related criticality. This may be due to the simplified nature of the analysis, such as neglecting combustion related volumetric expansion. COMSOL® simulations have shown that the simplified Schlichting-based analysis does not adequately predict the centerline velocity decay of air jets with initial air to fuel velocity ratios larger than around 0.2 – 0.5. However there is evidence that the analysis would more adequately predict the centerline velocity decay of jets with an initial uniform flow.

This current study has not proven a particular smoke point mechanism. It has shown that the smoke point depends on choice of coflow velocity and burner diameter; these factors cannot be assumed away as negligible. The coflow jet flame geometry is perhaps not tractable enough to lend itself to fundamental analysis of sooting phenomena. Given that a smoke point depends on a large number of inputs, more rigorous controls would be necessary to isolate particular factors. It is hoped;

however, given the results shown and the hypotheses presented, a more defined experimental procedure could be developed to directly influence and measure residence times, formation rates, and oxidation rates as they relate to the smoke point and sooting phenomena.

Chapter 6. Appendices

6.1. Pixel-Length Correlations

For microgravity SPICE flames obtained from screenshots from the downlinked video. Source indicates the whether video had been re-encoded in x264 format and the initial source. The axial pixel number is correlated with markings on a reference image of a ruler placed along the centerline of the module. Slope, *m*, is the change in scale distance over number of pixels. Intercept, *b*, is the scale distance at pixel zero (lower pixel numbers occur near the tip of the flame because of camera orientation). Table 6.1 presents the used correlations.

Table 6.1. Pixel number to scale distance correlations for smoke point images for SPICE microgravity flames.

Day of Year	45	48	48	52	55	58	119
Source	x264, DVD	x264, DVD	PNG	x264, DVD	x264, DVD	x264, DVD	x264, DVD
m, mm	-0.2297	-0.2333	-0.2021	-0.2297	-0.2307	-0.2258	-0.2239
b, mm	119.69	121.77	111.20	119.69	121.23	119.23	118.21

Day of Year	119	136	167	168	173	174	174
Source	x264, DVCAM	x264, DVD	x264, DVD	x264, DVD	x264, DVD	x264, DVD	x264, DVCAM
m, mm	-0.2298	-0.2273	-0.2299	-0.2298	-0.2259	-0.2300	-0.2298
b, mm	119.42	118.12	119.85	119.77	118.07	119.44	119.42

For the normal gravity flames obtained with the SPICE equipment, a similar process was followed except the source images are from the Nikon™ still camera. This single correlation is shown in Figure 6.1.

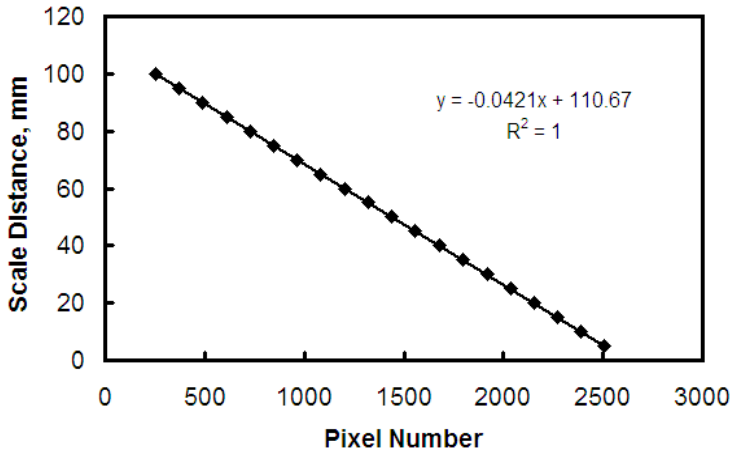

Figure 6.1. Pixel number to length scale distance correlation for all images obtained from Nikon still camera for normal gravity flames obtained with the SPICE module.

A slightly difference procedure was followed for the flame images obtained from the unconfined coflow burner. The axial pixel number at the center of the fuel jet exit was measured and taken as the zero datum. The flame tip axial pixel number is measured. The difference is taken and can be converted to a length with the following correlations given in Table 6.2. There were several different correlations for propane depending on the coflow velocity for which the image was taken at. The camera had been moved between shots.

Table 6.2. Pixel length correlations for obtaining scale distance for unconfined coflow smoke points.

	Ethylene 1	Propane 1	Propane 2	Propane 3	Propylene
m, mm	0.05774	0.05774	0.06523	0.06522	0.06522
b, mm	-0.1286	-0.1286	-0.0649	0.1589	0.1589
u_a *range, cm/s*	7.7 - 49	15 - 26	31.9	40 - 50	4.4 - 20

6.2. *Fuel Rotameter Correlation*

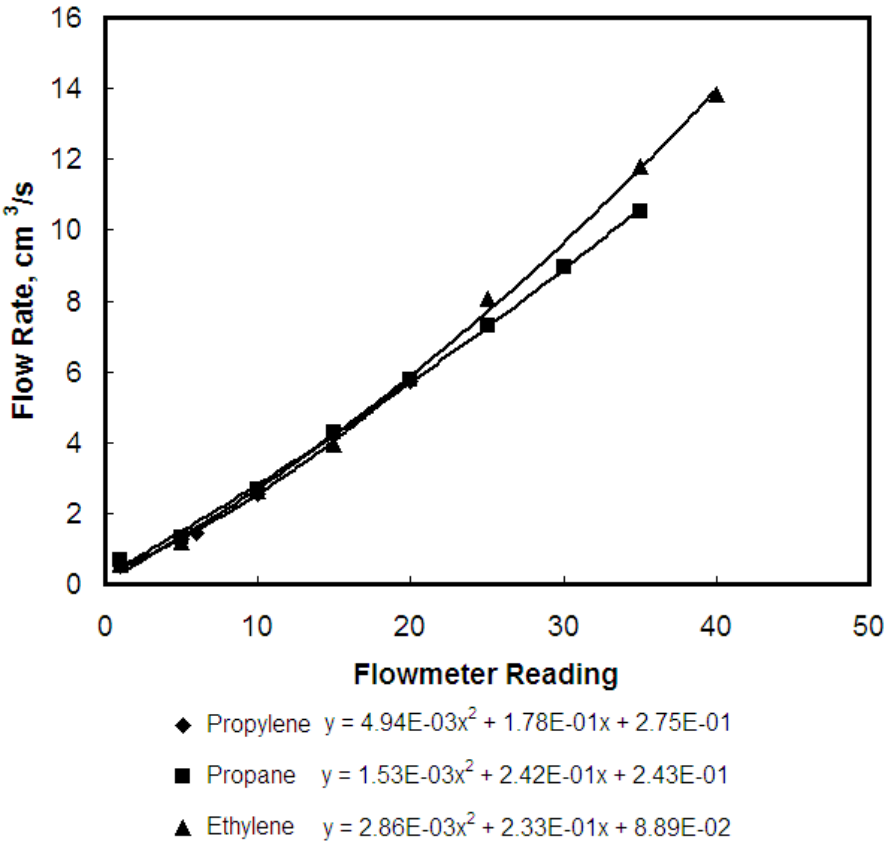

Figure 6.2. Correlation between rotameter reading and volumetric flow rate for fuel gases propylene, propane, and ethylene.

6.3. *Normal Gravity Smoke Point Results*

Table 6.3. Smoke points and measurements for normal gravity smoke points obtained from SPICE module.

Test Matrix Number	Fuel	Nozzle ID (mm)	Coflow Velocity (cm/s)	Mass Fuel Flow (mg/s)	Mean Fuel Velocity (cm/s)	Mean Smoke Height (mm)
37	75% C_3H_6	1.600	38.27	1.601	49.82	34.62
39	75% C_3H_6	1.600	57.08	1.870	58.19	38.64
41	75% C_3H_6	1.600	18.53	1.306	40.65	28.67
43	75% C_3H_6	0.764	38.27	2.407	328.71	55.23
47	75% C_3H_6	0.764	18.53	2.151	293.75	51.95
55	50% C_3H_6	1.600	39.21	3.068	105.07	48.88
57	50% C_3H_6	1.600	58.02	3.602	123.38	56.61
59	50% C_3H_6	1.600	19.47	2.645	90.61	43.05
73	100% C_3H_6	1.600	42.03	1.132	32.28	28.70
75	100% C_3H_6	1.600	59.90	1.346	38.39	33.83
77	100% C_3H_6	1.600	20.41	0.894	25.48	23.51
79	100% C_3H_6	0.764	39.21	1.406	175.89	38.78
81	100% C_3H_6	0.764	55.20	1.608	201.23	42.40
83	100% C_3H_6	0.764	18.53	1.203	150.55	34.32
89	100% C_3H_6	0.406	20.41	2.716	1201.08	83.09

Table 6.4. Smoke point measurements from unconfined coflow burner.

Fuel	Initial Coflow Velocity (cm/s)	Initial Fuel Velocity (cm/s)	Fuel Mass Flow Rate (mg/s)	Smoke Height (mm)	Air Stream Fr	Fuel Stream Fr
C_3H_8	15.43	2.480	6.668	129.86	9.35E-03	2.41E-04
C_3H_8	20.00	2.480	6.668	127.94	1.59E-02	2.45E-04
C_3H_8	25.27	2.576	6.926	131.60	2.47E-02	2.57E-04
C_3H_8	31.86	2.633	7.082	134.66	3.84E-02	2.62E-04
C_3H_8	40.07	2.808	7.552	150.64	5.43E-02	2.67E-04
C_3H_8	45.24	2.965	7.973	159.64	6.54E-02	2.81E-04
C_3H_8	49.35	3.064	8.239	164.04	7.57E-02	2.92E-04
C_2H_6	7.70	2.937	5.025	92.87	3.26E-03	4.73E-04
C_2H_6	11.38	2.828	4.840	87.17	7.58E-03	4.68E-04
C_2H_6	15.49	2.742	4.692	82.94	1.47E-02	4.62E-04
C_2H_6	20.12	2.657	4.546	80.67	2.56E-02	4.46E-04
C_2H_6	25.47	2.678	4.583	80.98	4.08E-02	4.52E-04
C_2H_6	31.93	2.446	4.186	76.20	6.82E-02	4.00E-04
C_2H_6	41.76	2.488	4.257	74.66	1.19E-01	4.23E-04
C_2H_6	45.18	2.384	4.079	71.01	1.47E-01	4.08E-04
C_2H_6	49.31	2.138	3.657	65.81	1.88E-01	3.54E-04
C_3H_6	4.39	0.580	1.489	29.20	3.36E-03	5.87E-05
C_3H_6	7.87	0.552	1.417	26.94	1.17E-02	5.76E-05
C_3H_6	11.54	0.416	1.066	24.12	2.82E-02	3.65E-05
C_3H_6	15.66	0.350	0.898	23.68	5.27E-02	2.63E-05
C_3H_6	20.04	0.286	0.734	20.20	1.01E-01	2.06E-05

6.4. *Microgravity Flame Images*

Approximate burner tube location is indicated by a gray line. White scale line is approximate.

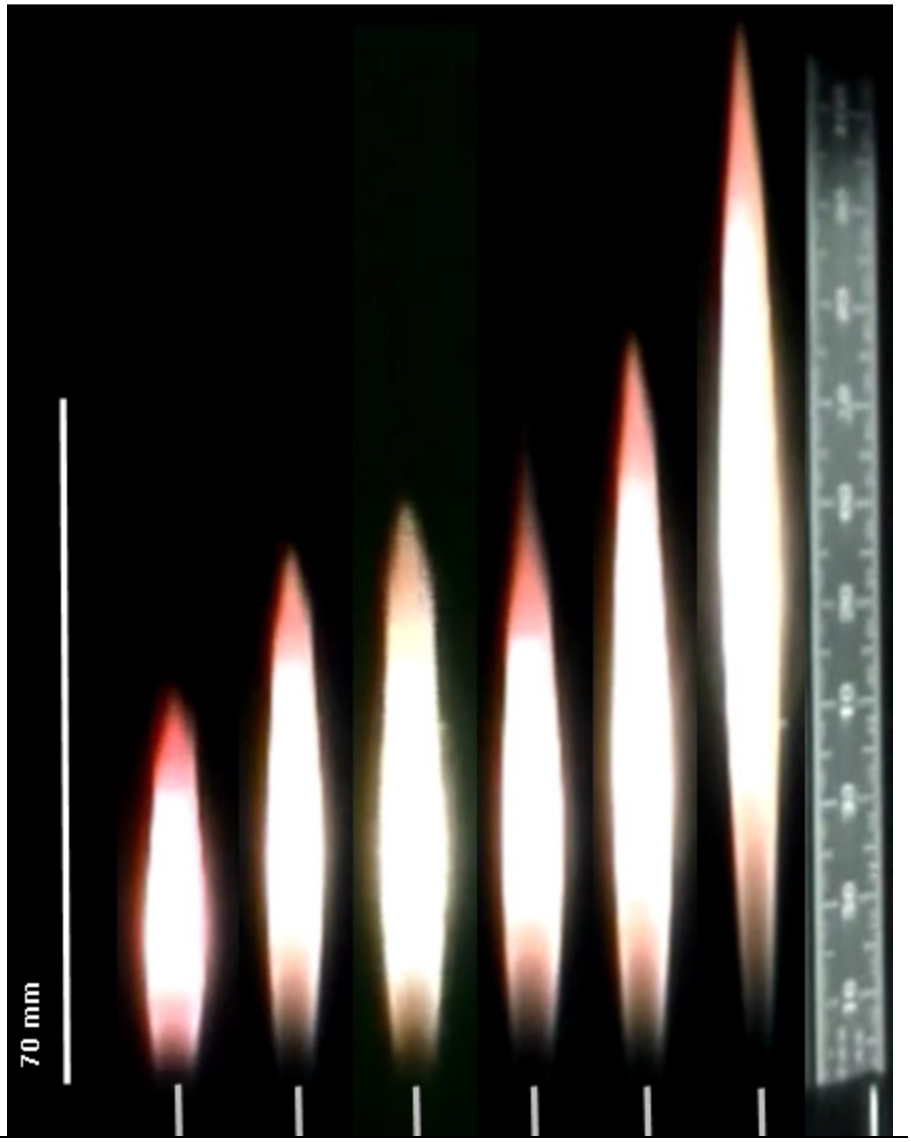

Fuel	C_2H_6	C_2H_6	C_2H_6	C_2H_6	C_2H_6	C_2H_6
Nozzle (mm)	1.600	1.600	1.600	1.600	1.60	0.762
Day of Year	45	45	45	45	45	45
GMT	15:48:47	14:37:56	09:50:28	14:50:32	15:03:15	17:28:09
Fuel Rate (mg/s)	1.627	2.406	2.426	2.452	3.313	3.894
Air Rate (cm/s)	18.53	33.57	36.39	39.21	58.02	17.59
Length (mm)	36.99	53.99	57.50	55.83	75.35	105.22

Figure 6.3. Stills of smoke point flames and measurements for ethylene. Ruler image taken for reference is also shown.

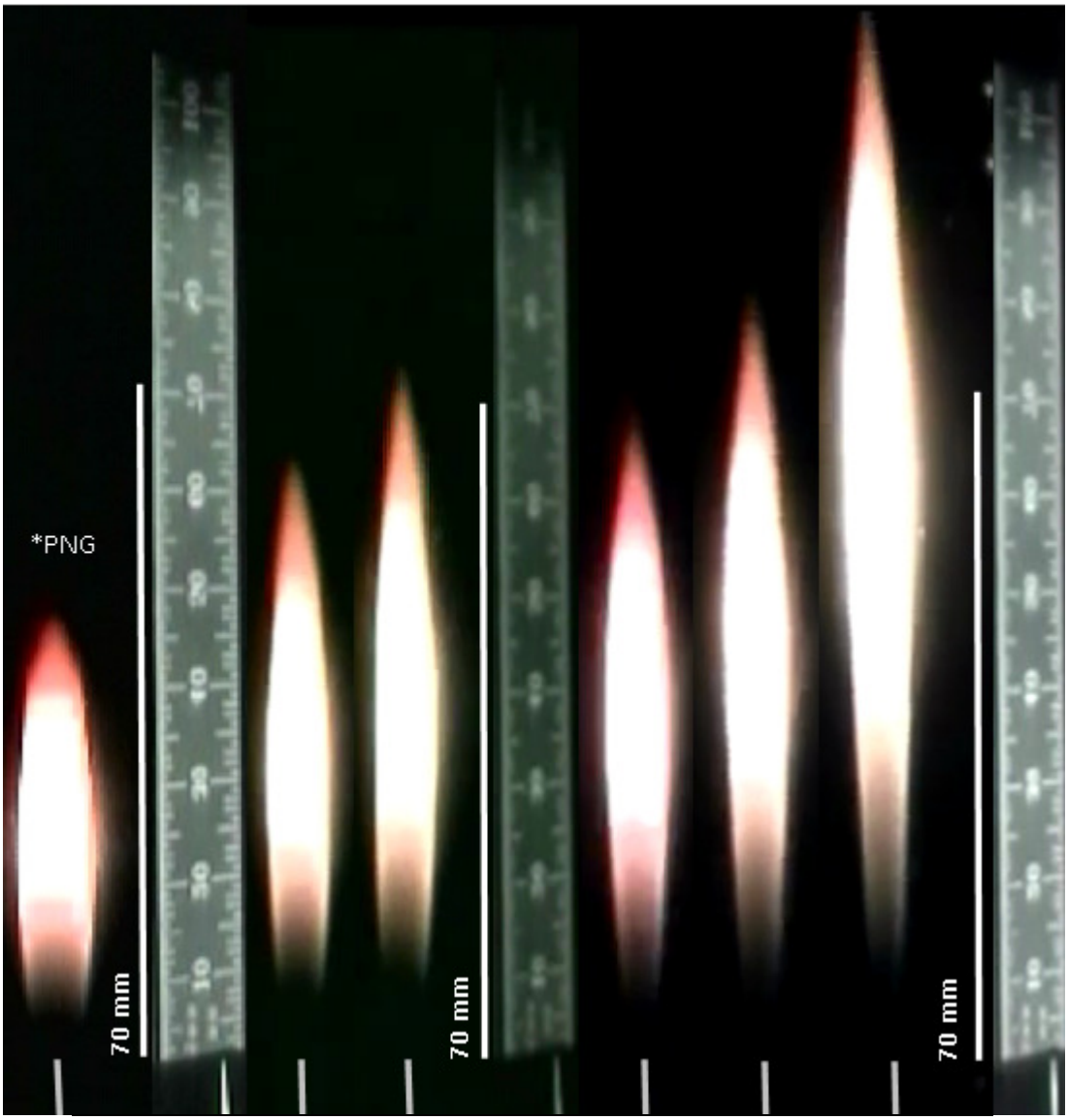

Fuel	C_3H_8	C_3H_8	C_3H_8	C_3H_8	C_3H_8	C_3H_8
Nozzle (mm)	1.600	1.600	1.600	0.762	0.762	0.762
Day of Year	48	48	48	52	52	52
GMT	17:45:17	17:12:08	16:54:27	11:49:43	11:43:05	11:39:28
Fuel Rate (mg/s)	1.798	2.521	3.025	2.258	2.631	3.836
Air Rate (cm/s)	22.29	36.39	44.85	16.65	21.35	33.57
Length (mm)	45.52	61.12	71.38	64.33	75.58	105.45

Figure 6.4. Stills of smoke point flames and measurements for propane. Ruler image taken for reference is also shown.

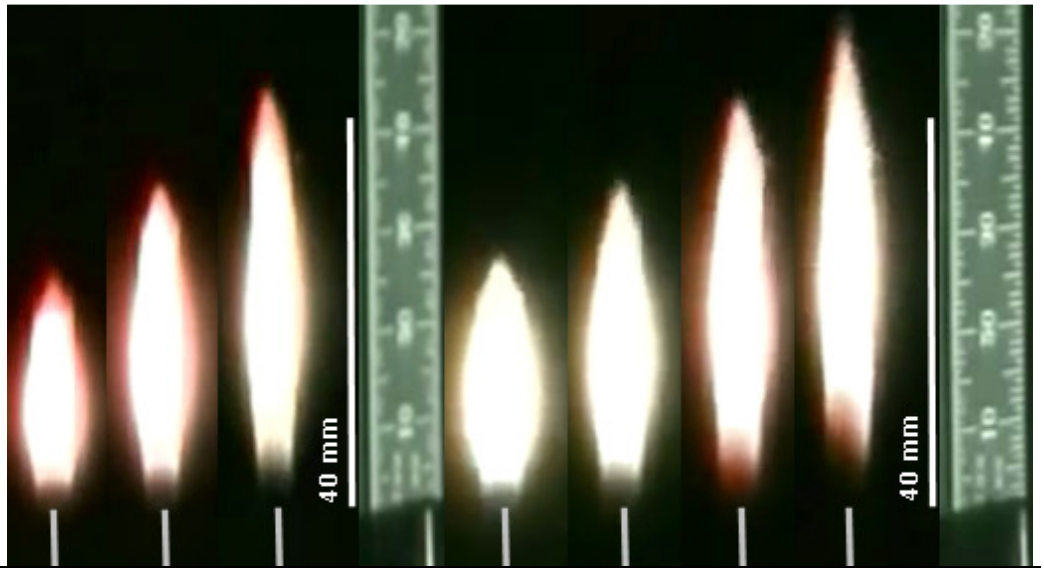

Fuel	50% C_3H_6	50% C_3H_6	50% C_3H_6	50% C_3H_6	50% C_3H_6	50% C_3H_6	50% C_3H_6
Nozzle (mm)	1.600	1.600	1.600	1.600	1.600	1.600	1.600
Day of Year	55	55	55	167	167	167	167
GMT	08:26:28	09:37:29	09:40:13	09:23:36	09:32:48	09:41:01	09:45:36
Fuel Rate (mg/s)	1.449	2.195	2.885	1.618	2.181	2.913	3.293
Air Rate (cm/s)	11.01	26.05	40.15	12.89	26.05	40.15	48.61
Length (mm)	22.12	32.50	41.73	26.52	33.41	42.38	49.51

Figure 6.5. Stills of smoke points and measurements for 50% propylene. Ruler image taken for reference is also shown.

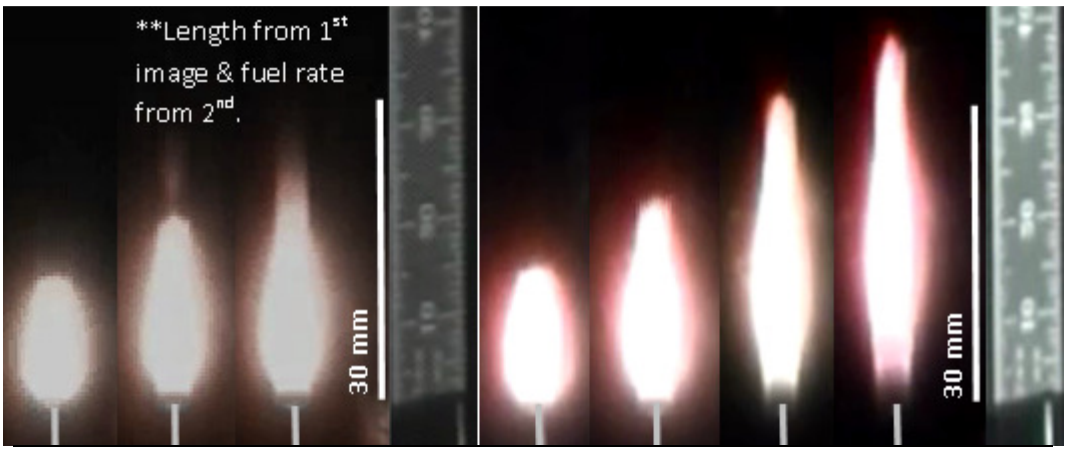

Fuel	75% C_3H_6	75% C_3H_6	75% C_3H_6	75% C_3H_6	75% C_3H_6	75% C_3H_6
Nozzle (mm)	1.600	1.600	1.600	1.600	1.600	1.600
Day of Year	119	119	52	52	52	52
GMT	10:29:30	10:38:53	16:09:59	16:23:20	16:26:48	16:14:10
Fuel Rate (mg/s)	0.627	0.922	0.640	1.012	1.498	1.908
Air Rate (cm/s)	12.89	26.99	12.89	28.87	51.34	64.60
Length (mm)	14.16	20.36	14.47	21.14	31.70	37.68

Figure 6.6. Stills of smoke points and measurements for 75% propylene, 1.6 mm burner. Ruler image taken for reference is also shown.

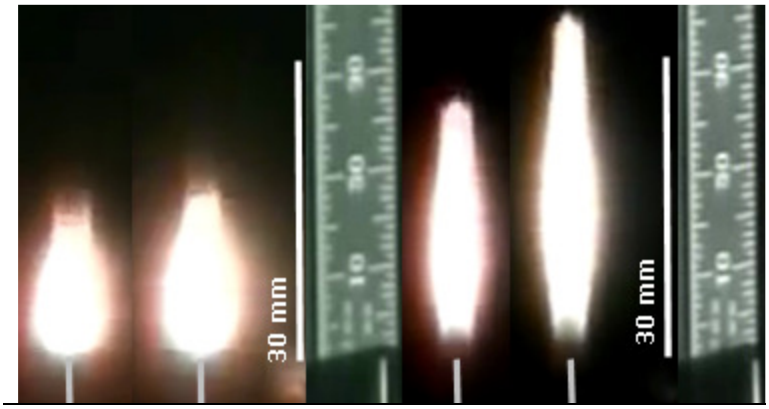

Fuel	75% C_3H_6	75% C_3H_6	75% C_3H_6	75% C_3H_6
Nozzle (mm)	1.600	1.600	1.600	1.600
Day of Year	136	136	173	173
GMT	15:57:52	15:53:36	11:09:27	10:38:23
Fuel Rate (mg/s)	0.666	0.781	1.344	1.882
Air Rate (cm/s)	16.65	23.23	42.03	58.96
Length (mm)	15.61	17.88	26.65	35.84

Figure 6.7. Stills of smoke points and measurements for additional 75% propylene, 1.6 mm burner points. Ruler image taken for reference is also shown.

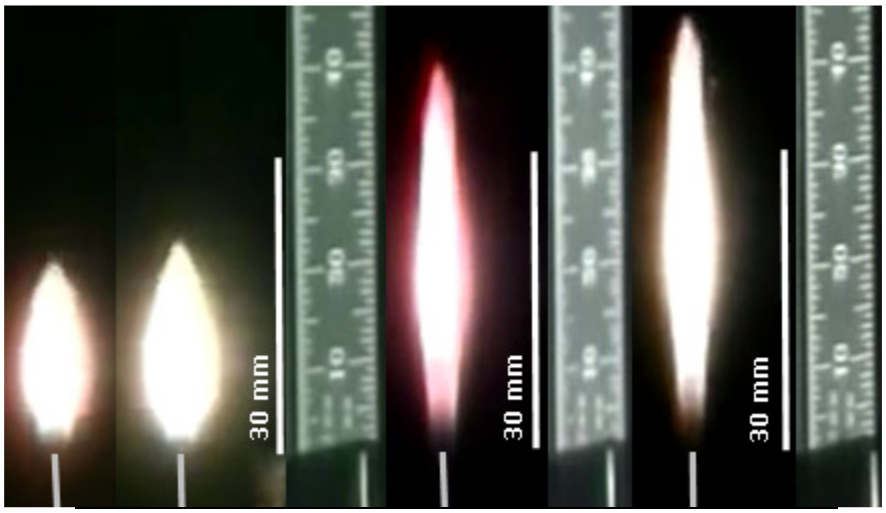

Fuel	75% C_3H_6	75% C_3H_6	75% C_3H_6	75% C_3H_6
Nozzle (mm)	0.762	0.762	0.762	0.762
Day of Year	136	136	52	173
GMT	17:21:52	17:23:30	17:30:19	12:40:44
Fuel Rate (mg/s)	0.871	0.896	1.908	1.998
Air Rate (cm/s)	14.77	14.77	37.33	38.27
Length (mm)	20.15	21.97	39.52	43.98

Figure 6.8. Stills of smoke points and measurements for 75% propylene, 0.762 mm burner. Rule image taken for reference is also shown.

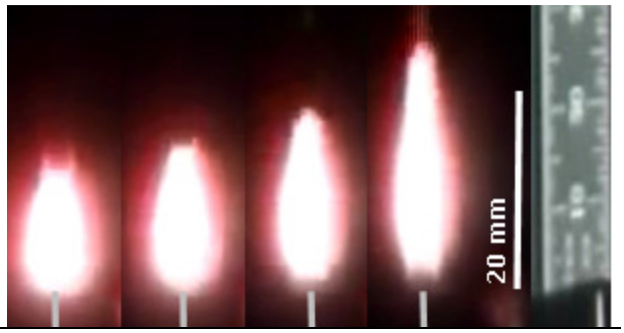

Fuel	C_3H_6	C_3H_6	C_3H_6	C_3H_6
Nozzle (mm)	1.600	1.600	1.600	1.600
Day of Year	58	58	58	58
GMT	09:38:07	09:44:41	09:47:29	09:55:32
Fuel Rate (mg/s)	0.441	0.548	0.727	1.001
Air Rate (cm/s)	9.13	22.29	33.57	51.43
Length (mm)	13.99	15.79	19.63	25.73

Figure 6.9. Stills of smoke points and measurements for propylene, 1.6 mm burner. Rule image taken for reference is also

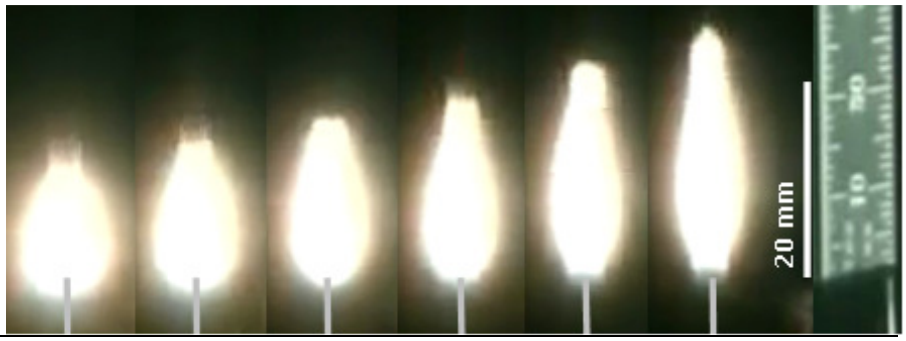

Fuel	C_3H_6	C_3H_6	C_3H_6	C_3H_6	C_3H_6	C_3H_6
Nozzle (mm)	1.600	1.600	1.600	1.600	1.600	1.600
Day of Year	174	174	174	174	174	174
GMT	10:49:00	10:46:19	11:05:39	11:25:31	11:22:35	11:14:07
Fuel Rate (mg/s)	0.393	0.572	0.715	0.762	0.965	1.168
Air Rate (cm/s)	10.07	20.41	29.81	40.15	46.73	57.08
Length (mm)	13.42	15.49	17.57	19.40	23.08	26.53

Figure 6.10. Stills of smoke points and measurements for additional propylene, 1.6 mm burner points. Ruler image taken for reference is also shown.

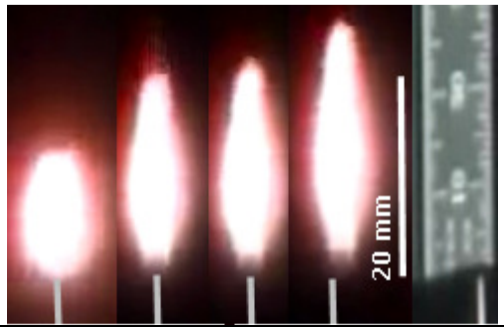

Fuel	C_3H_6	C_3H_6	C_3H_6	C_3H_6
Nozzle (mm)	0.762	0.762	0.762	0.762
Day of Year	58	58	58	58
GMT	10:13:37	12:45:55	10:36:31	10:41:26
Fuel Rate (mg/s)	0.488	0.762	0.822	1.001
Air Rate (cm/s)	7.24	26.99	28.87	41.09
Length (mm)	14.21	21.67	22.80	26.63

Figure 6.11. Stills of smoke points and measurements for propylene, 0.762 mm burner. Ruler image taken for reference is also shown.

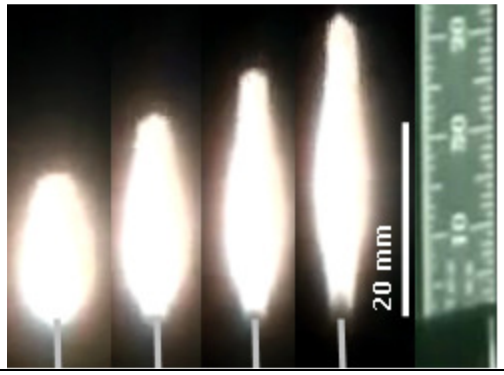

Fuel	C_3H_6	C_3H_6	C_3H_6	C_3H_6
Nozzle (mm)	0.762	0.762	0.762	0.762
Day of Year	174	174	174	174
GMT	12:36:49	12:34:40	12:47:37	12:44:11
Fuel Rate (mg/s)	0.524	0.739	0.953	1.322
Air Rate (cm/s)	12.89	24.17	31.69	50.49
Length (mm)	15.95	21.93	26.30	31.82

Figure 6.12. Stills of smoke points and measurements for additional propylene, 0.762 mm burner points. Ruler image taken for reference is also shown.

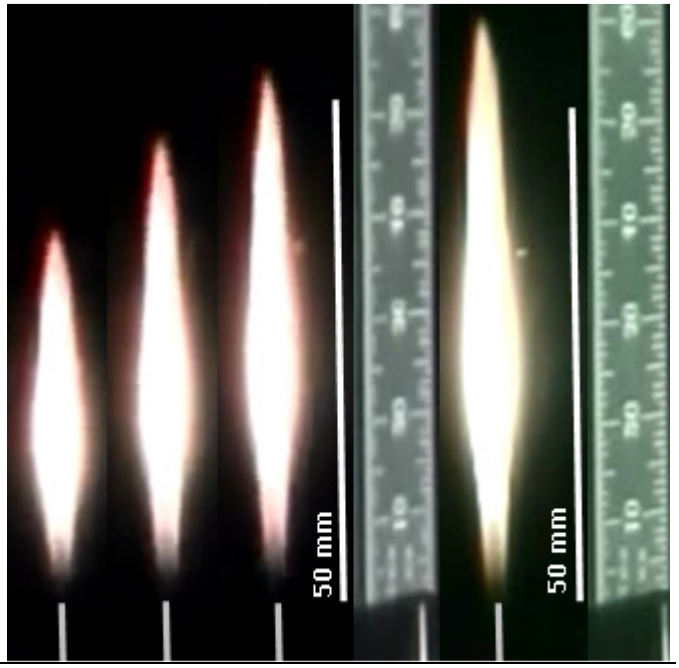

Fuel	C_3H_6	C_3H_6	C_3H_6	C_3H_6
Nozzle (mm)	0.4064	0.4064	0.4064	0.4064
Day of Year	58	58	58	174
GMT	11:23:35	11:26:27	11:32:14	11:48:02
Fuel Rate (mg/s)	1.096	1.346	1.620	1.727
Air Rate (cm/s)	5.36	14.77	26.99	10.07
Length (mm)	37.70	46.96	53.28	59.19

Figure 6.13. Stills of smoke points measurements for propylene, 0.4064 mm burner. Ruler image taken for reference is also shown.

Bibliography

[1] Mokdad, A. H., Marks, J. S., Stroup, D. F., and Gerberding, J. L., "Actual Causes of Death in the United States, 2000," *The Journal of the American Medical Association*, Vol. 291, No. 10, 2004, pp. 1238-1245.

[2] Ramanathan, V., and Carmichael, G., "Global and Regional Climate Change Due to Black Carbon," *Nature Geoscience*, Vol. 1, No. 4, 2008, pp. 221-227.

[3] Purser, D. A., "Assessment of Hazards to Occupants from Smoke, Toxic Gases, and Heat," *SFPE Handbook of Fire Protection Engineering*, 4th ed., edited by DiNenno, P. J., et al., National Fire Protection Association, Quincy, MA, 2008, pp. 2-96-2-193.

[4] Schug, K. P., Manheimer-Timnat, Y., Yaccarino, P., and Glassman, I., "Sooting Behavior of Gaseous Hydrocarbon Diffusion Flames and the Influence of Additives," *Combustion Science and Technology*, Vol. 22, No. 5/6, 1980, pp. 235-250.

[5] Markstein, G. H., "Correlations for Smoke Points and Radiant Emission of Laminar Hydrocarbon Diffusion Flames," *Twenty-Second Symposium (International) on Combustion*, The Combustion Institute, Pittsburgh, PA, 1988, pp. 363-370.

[6] Sivathanu, Y. R., and Faeth, G. M., "Temperature / Soot Volume Fraction Correlations in the Fuel-Rich Region of Buoyant Turbulent Diffusion Flames," *Combustion and Flame*, Vol. 81, No. 2, 1990, pp. 133-149.

[7] Lin, K.-C. and Faeth, G. M., "Hydrodynamic Suppression of Soot Emissions in Laminar Diffusion Flames," *Journal of Propulsion and Power*, Vol. 12, No. 1, 1996, pp. 10-17.

[8] Berry, T. L., and Roberts, W. L., "Measurement of Smoke Point in Velocity-Matched Coflow Laminar Diffusion Flames with Pure Fuels at Elevated Pressures," *Combustion and Flame*, Vol. 145, No. 3, 2006, pp. 571-578.

[9] Allan, K. M., Kaminski, J. R., Bertrand, J. C., Head, J., and Sunderland, P. B., "Laminar Smoke Points of Wax Candles," *Combustion Science and Technology*, Vol. 181, No. 5, 2009, pp. 800-811.

[10] Kent, J. H., "Turbulent Diffusion Flame Sooting – Relationship to Smoke-Point Tests," *Combustion and Flame*, Vol. 67, No. 3, 1987, pp. 223-233.

[11] Markstein, G. H., "Relationship Between Smoke Point and Radiant Emission from Buoyant Turbulent and Laminar Diffusion Flames," *Twentieth Symposium (International) on Combustion*, The Combustion Institute, Pittsburgh, PA, 1984, pp. 1055-1061.

[12] Yang, Y., Boehman, A. L., and Santoro, R. J., "A Study of Jet Fuel Sooting Tendency Using the Threshold Sooting Index (TSI) Model," *Combustion and Flame*, Vol. 149, No. 1-2, 2007, pp. 191-205.

[13] Delichatsios, M. A., "Smoke Yields from Turbulent Buoyant Jet Flames," *Fire Safety Journal*, Vol. 20, No. 4, 1993, pp. 299-311.

[14] Lautenberger, C. W., de Ris, J. L., Dembsey, N. A., Barnett, J. R., and Baum, H. R., "A Simplified Model for Soot Formation and Oxidation in CFD Simulation of Non-Premixed Hydrocarbon Flames," *AIAA Journal*, Vol. 40, No. 2, 2005, pp. 141-176.

[15] Linteris, G. T., and Rafferty, I. P., "Flame Size, Heat Release, and Smoke Points in Materials Flammability," *Fire Safety Journal*, Vol. 43, No. 6, 2008, pp. 442-450.

[16] Faeth, G. M., "Laminar and Turbulent Gaseous Diffusion Flames," *Microgravity Combustion: Fire in Freefall*, edited by H. D. Ross, Combustion Treatise, Academic Press, San Diego, CA, 2001, pp. 83-182.

[17] Harris, S. J. and Weiner, A. M., "Surface Growth of Soot Particles in Premixed Ethylene/Air Flames," *Combustion Science and Technology*, Vol. 31, No. 3, 1983, pp. 155-167.

[18] Harris, S. J., and Weiner, A. M., "Some Constraints on Soot Particle Inception in Premixed Ethylene Flames," *Twentieth Symposium (International) on Combustion*, The Combustion Institute, Pittsburgh, PA, 1984, pp. 969-978.

[19] Kent, J. H., Jandes, H. and Wagner H.Gg., "Soot Formation in a Laminar Diffusion Flame," *Eighteenth Symposium (International) on Combustion, The Combustion Institute*, Pittsburgh, PA, 1981, pp. 1117-1126.

[20] Kent J. H. and Wagner H.G.g, "Soot Measurements in Laminar Ethylene Diffusion Flames," *Combustion and Flame*, Vol. 47, No. 1982, pp. 53-65.

[21] Santoro, R. J., Semerjian, H. G., and Dobbins, R. A., "Soot Particle Measurements in Diffusion Flames," *Combustion and Flame*, Vol. 51, 1983, pp. 203-218.

[22] Santoro, R. J., Yeh, T. T., Horvath, J. J., and Semerjian, H. G., "The Transport and Growth of Soot Particles in Laminar Diffusion Flames," *Combustion Science and Technology*, Vol. 53, No. 2, 1987, pp. 89-115.

[23] Gomez, A., Littman, M., Glassman, I., "Comparative Study of Soot Formation on the Centerline of Asixymmetric Laminar Diffusion Flames: Fuel and Temperature Effects," *Combustion and Flame*, Vol. 70, No. 2, 1987, pp. 225-241.

[24] Sunderland, P. B., and Faeth, G. M., "Soot Formation in Hydrocarbon / Air Laminar Jet Flames," *Combustion and Flame*, Vol. 105, No. 1-2, 1996, pp. 132-146.

[25] Kent, J. H., and Wagner, H. Gg., "Why Do Diffusion Flames Emit Smoke," *Combustion Science and Technology*, Vol. 41, No. 5/6, 1984, pp. 245-269.

[26] Urban, D. L., Yuan, Z.-G., Sunderland, P. B., Linteris, G. T., Voss, J. E., Lin, K.-C., Dai, Z., Sun, K., and Faeth, G. M., "Structure and Soot Properties of Nonbuoyant Ethylene/Air Laminar Jet Diffusion Flames," *AIAA Journal*, Vol. 36, No. 8, 1998, pp. 1346-1360.

[27] Lautenberger, C. W., De Ris, J. L., Dembsey, N. A., Barnett, J. R., Baum, H. R., "A Simplified Model for Soot Formation and Oxidation in CFD Simulation of Non-Premixed Hydrocarbon Flames," *Fire Safety Journal*, Vol. 40, No. 2, 2005, pp. 141-176.

[28] Markstein, G. H., "Radiant Emission and Smoke Points for Laminar Diffusion Flames of Fuel Mixtures," *Twenty-First Symposium (International) on Combustion*, The Combustion Institute, Pittsburgh, PA, 1986, pp. 1107-1114.

[29] Frenklach, M., "Reaction Mechanism of Soot Formation in Flames," *Physical Chemistry Chemical Physics*, Vol. 4, No. 11, 2002, pp. 2028-2037.

[30] Mansurov, Z. A., "Soot Formation in Combustion Processes (Review)," *Combustion, Explosion, and Shock Waves*, Vol. 41, No. 6, 2005, pp. 727-744.

[31] Glassman, I., "Soot Formation in Combustion Processes," *Twenty-Second Symposium (International) on Combustion*, The Combustion Institute, Pittsburgh, PA, 1988, pp. 295-311.

[32] Richter, H. and Howard J. B., "Formation of Polycyclic Aromatic Hydrocarbons and Their Growth to Soot – A Review of Chemical Reaction Pathways," *Progress in Energy and Combustion Science*, Vol. 26, No. 4-6, 2000, pp. 565-608.

[33] Stanmore B. R. Brilhac, J. F., and Gilot, P., "The Oxidation of Soot: A Review of Experiments, Mechanisms and Models," *Carbon*, Vol. 39, No. 15, 2001, pp. 2247-2268.

[34] Schalla, R. L. and McDonald, G. E., "Mechanism of Soot Formation in Flames," *Fifth Symposium (International) on Combustion*, The Combustion Institute, Pittsburgh, PA, 1955.

[35] Axelbaum, R. L. and Law, C. K., "Soot Formation and Inert Addition in Diffusion Flames," *Twenty-Third Symposium (International) on Combustion*, The Combustion Institute, Pittsburgh, PA, 1990, pp. 1517-1523.

[36] Glassman, I., "Sooting Laminar Diffusion Flames: Effect of Dilution, Additives, Pressure, and Microgravity," *Twenty-Seventh Symposium (International) on Combustion*, The Combustion Institute, Pittsburgh, PA, 1998, pp. 1589-1596.

[37] Glassman, I., "Soot Formation in Combustion Processes," *Twenty-Second Symposium (International) on Combustion*, The Combustion Institute, Pittsburgh, PA, 1988, pp. 295-311.

[38] Sunderland, P. B., Mortazavi, S., Faeth, G. M., and Urban, D. L., "Laminar Smoke Points of Nonbuoyant Jet Diffusion Flames," *Combustion and Flame*, Vol. 96, No. 1-2, 1994, pp. 97-103.

[39] Urban, D. L., Yuan, Z.-Y., Sunderland, P. B., Lin, K.-C., Dai, Z., and Faeth, G. M., "Smoke-Point Properties of Non-Buoyant Round Laminar Jet Diffusion Flames," *Proceedings of the Combustion Institute*, Vol. 28, No. 2, 2000, pp. 1965-1972.

[40] Berry Yelverton, T. L., Roberts, W. L., "Effect of Dilution, Pressure, and Velocity on Smoke Point in Laminar Jet Flames," *Combustion Science and Technology*, Vol. 180, No. 7, 2008, pp. 1334-1346.

[41] Jeon, B. H., Fujita, O., Nakamura, Y., and Ito, H., "Effect of Co-Axial Flow Velocity on Soot Formation in a Laminar Jet Diffusion Flame under Microgravity," *Journal of Thermal Science and Technology*, Vol. 2, No. 2, 2007, pp. 281-290.

[42] Lin, K.-C. and Faeth, G. M., "Shapes of Nonbuoyant Round Luminous Laminar-Jet Diffusion Flames in Coflowing Air," *AIAA Journal*, Vol. 37, No. 6, 1999, pp. 750-765.

[43] Lin, K.-C., Faeth, G. M., Sunderland, P. B., Urban, D. L., and Yuan, Z.-G., "Shapes of Buoyant and Nonbuoyant Laminar Jet Diffusion Flames," *Combustion and Flame*, Vol. 116, No. 3, 1999, pp. 415-431.
[44] Dai, Z. and Faeth, G. M., "Hydrodynamic Suppression of Soot Formation in Laminar Coflowing Jet Diffusion Flames," *Proceedings of the Combustion Institute*, Vol. 28, No. 2, 2000, pp. 2085-2095.
[45] Spalding D. B., *Combustion and Mass Transfer*, Pergamon, New York, 1979, pp. 185-195.
[46] Mahalingam, S., Ferziger, J. H., and Cantwell, B. J., "Self-Similar Diffusion Flame," *Combustion and Flame*, Vol. 82, No. 2, 1990, pp. 231-234.
[47] Delichatsios, M. A., "A Phenomenological Model for Smoke-Point and Soot Formation in Laminar Flames," *Combustion Science and Technology*, Vol. 100, No. 1-6, 1994, pp. 293-298.
[48] Beji, T., Zhang, J. P., and Delichatsios, M., "Determination of Soot Formation Rate from Laminar Smoke Point Measurements," *Combustion Science and Technology*, Vol. 180, No. 5, 2008, pp. 927-940.
[49] Andrade, E. N. da C. and Tsien, L. C., "The Velocity-Distribution in a Liquid-into-Liquid Jet," *Proceedings of the Physical Society*, Vol. 49, 1937, pp. 381-391.
[50] Arulraja, M., Rankin, G. W., and Sridhar, K., "Maximum Velocity Decay in a Submerged Laminar Jet Issuing from a 'Long Tube'," *Transactions of the Canadian Society of Mechanical Engineering*, Vol. 7, No. 1, 1983, pp. 41-43.
[51] Abramovich, S. and Solan, A., "The Initial Development of a Submerged Laminar Round Jet," *Journal of Fluid Mechanics*, Vol. 59, No. 4, 1973, pp. 791-801.
[52] Rankin, G. W., Sridhar, K., Arulraja, M., and Kumar, K. R., "An Experimental Investigation of Laminar Axisymmetric Submerged Jets," *Journal of Fluid Mechanics*, Vol. 133, 1983, pp. 217-231.
[53] Lee, D. S., Kihm, K. D., and Chung, S. H., "Analytical Solutions for the Developing Jet From a Fully-Developed Laminar Tube Flow," *Journal of Fluids Engineering*, Vol. 119, No. 3, 1997, pp. 716-718.
[54] Kwon, S. J. and Seo, I. W., "Reynolds Number Effects on the Behavior of a Non-Buoyant Round Jet," *Experiments in Fluids*, Vol. 38, 2005, pp. 801-812.
[55] Nickels, T. B. and Perry, A. E., "An Experimental and Theoretical Study of the Turbulent Coflowing Jet," *Journal of Fluid Mechanics*, Vol. 309, 1996, pp. 157-182.
[56] Chan, C. H. C. and Lam, K. M., "Centerline Velocity Decay of a Circular Jet in a Counterflowing Stream," *Physics of Fluids*, Vol. 10, No. 3, 1998, pp. 637-644.
[57] Xia, L. P. and Lam, K. M., "Velocity and Concentration Measurements in Initial Region of Submerged Round Jets in Stagnant Environments and in Coflow," *Journal of Hydro-environment Research*, Vol. 3, 2009, pp. 21-34.
[58] Schlichting, H. and Gersten, K., "Boundary-Layer Theory," 8th Ed., Spring-Verlag, New York, 2003
[59] Revuelta A., Sánchez, A. L., and Liñán, A., "The Virtual Origin as a First-Order Correction for the Far-Field Description of Laminar Jets," *Physics of Fluids*, Vol. 14, No. 6, 2002, pp. 1821-1824.
[60] Lee, J., Won, S. H., Jin, S., Chung, S. H., "Lifted Flames in Laminar Jets of Propane in Coflow Air," *Combustion and Flame*, Vol. 135, No. 4, 2003, pp. 449-462.
[61] Rajaratnam, N., "Turbulent Jets," Elsevier Scientific Publishing, Amsterdam, 1976.